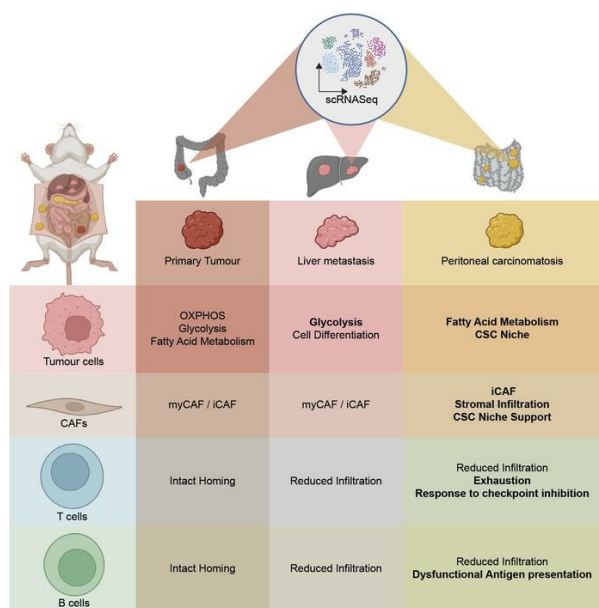# Single-cell deconvolution reveals high lineage- and location-dependent heterogeneity in mesenchymal multivisceral stage IV colorectal cancer

Christopher Berlin, … , Philipp A. Holzner, Rebecca Kesselring

Graphical abstract

Single-cell deconvolution reveals high lineage- and location-dependent heterogeneity in mesenchymal multivisceral stage IV colorectal cancer

Christopher Berlin[1, 2, 3, 4 *], Bernhard Mauerer[1, 2, 3], Pierre Cauchy[1,2,3#], Jost Luenstedt[1,4#], Roman Sankowski[5, 6#], Lisa Marx[1#], Reinhild Feuerstein[1], Luisa Schaefer[1], Florian R. Greten[3, 7], Marina Pesic[7], Olaf Groß[5, 8], Marco Prinz[5, 8, 9], Naomi Ruehl[1], Laura Miketiuk[1], Dominik Jauch[1], Claudia Laessle[1,10], Andreas Jud[1], Esther A. Biesel[1], Hannes Neeff[1], Stefan Fichtner-Feigl[1, 2, 3], Philipp A. Holzner[1], Rebecca Kesselring[1, 2, 3, *]

Affiliations:

[1] Department of General and Visceral Surgery, Faculty of Medicine, University of Freiburg; Freiburg, Germany.

[2] German Cancer Consortium (DKTK) partner site; Freiburg, Germany.

[3] German Cancer Research Center (DKFZ); Heidelberg, Germany.

[4] IMM-PACT Clinician Scientist Program, Faculty of Medicine, University of Freiburg; Freiburg, Germany.

[5] Institute of Neuropathology, Faculty of Medicine, University of Freiburg; Freiburg, Germany.

[6] Single-Cell Omics Platform Freiburg, Faculty of Medicine, University of Freiburg; Freiburg, Germany.

[7] Institute for Tumor Biology and Experimental Therapy, Georg-Speyer-Haus; Frankfurt/Main, Germany.

[8] Signalling Research Centres BIOSS and CIBSS, University of Freiburg; Freiburg, Germany.

[9] Center for Basics in NeuroModulation (NeuroModulBasics), Faculty of Medicine, University of Freiburg; Freiburg, Germany.

[10] EXCEL Excellent Clinician Scientist Program, Faculty of Medicine, University of Freiburg; Freiburg, Germany.

[#] These authors contributed equally.

Corresponding authors:

Dr. med. Dr. rer. nat. Christopher Berlin

Department of General and Visceral Surgery

Medical Center University Freiburg

Hugstetter Strasse 55

79106 Freiburg im Breisgau

Germany

Phone: +49 761 270 24010

email: christopher.berlin@uniklinik-freiburg.de

and

PD Dr. Rebecca Kesselring

Department of General and Visceral Surgery

Medical Center University Freiburg

Breisacher Strasse 115

79106 Freiburg im Breisgau

Germany

Phone: +49 761 270 77573

email: rebecca.kesselring@uniklinik-freiburg.de

Conflict of interest statement:

The authors have declared that no conflict of interest exists.

Running title: Molecular and cellular site-specific landscape of multivisceral CRC

Abstract

Metastasized colorectal cancer (CRC) is associated with a poor prognosis and rapid disease progression. Besides hepatic metastasis, peritoneal carcinomatosis is the major cause of death in UICC *(*Union for International Cancer Control) stage IV CRC patients. Insights into differential site-specific reconstitution of tumour cells and the corresponding tumour microenvironment are still missing. Here, we analysed the transcriptome of single cells derived from murine multivisceral CRC and delineated the inter-metastatic cellular heterogeneity regarding tumour epithelium, stroma and immune cells. Interestingly, we found an intercellular site-specific network of cancer associated fibroblasts and tumour epithelium during peritoneal metastasis as well as an autologous feed-forward loop in cancer stem cells. We furthermore deciphered a metastatic dysfunctional adaptive immunity by a loss of B cell dependent antigen presentation and consecutive effector T cell exhaustion. Furthermore, we demonstrated major similarities of this murine metastatic CRC model with human disease and -based on the results of our analysis- provided an auspicious site-specific immune modulatory treatment approach for stage IV CRC by intraperitoneal checkpoint inhibition.

Introduction

Colorectal cancer (CRC) is the second most diagnosed cancer in females and the third most common in males, with about 0.8 million deaths worldwide per year (1). Whereas primary CRC in early stages is mostly curable by surgery, mortality rates of metastatic cancer are still high (2). Therefore, it is critical to understand the entire multi-step process of metastasis, also considering a strong inter-metastatic heterogeneity between tumour locations, accounting for tumour-specific adaptations to local environments. While an immunosuppressive phenotype of the tumour microenvironment (TME) is already described for colorectal liver metastases (CRLM) (3-6), the inter-metastatic differential reconstitution of the TME in peritoneal carcinomatosis (PC) has not been investigated yet since appropriate mouse models mimicking human metastasis are still missing (7-11). Due to limitations of treatment options, PC is associated with the worst survival in CRC patients and occurs most frequently in a mesenchymal subtype of CRC, which is resembled by a consensus molecular subtype (CMS) 4 (12, 13). This molecular subtype is characterized by the poorest survival rate, represents ~ ¼ of CRC patients (14) and shows an immune-tolerant, inflamed TME (15). Hence, there is an urgent need to understand the molecular and cellular landscape during CRC metastasis to different metastatic locations without the influence of intermittent therapeutic interventions.

Here, we aim to understand the site-specific landscape of metastasized CRC by single-cell RNA-seq (scRNA-seq) using a surgical tumour organoid driven orthotopic CRC mouse model. Our analyses unravelled location-dependent epithelial, stromal and immunological changes during metastasis to the liver and the peritoneum. While we observed a self-sustaining metastatic stem cell niche in PC which was furthermore

supported by inflammatory fibroblasts, our data suggested an impaired anti-tumoural adaptive immunity during metastasis with a conversely enhanced effector function of innate immune cells. Our findings confirmed the proposed mouse model as a state-of-the-art model to study the molecular and cellular landscape of multivisceral CRC, resembling human metastasis. Additionally, we identified individual cellular compartments of the TME as promising therapeutic targets as we suggest a necessity for a site-specific adaptation of therapeutic approaches.

Results

A distinct cellular and functional landscape of murine primary CRC, liver metastases and peritoneal carcinomatosis

To set up an mouse model for the investigation of treatment-naïve hepatic and peritoneal metastasis of CRC, we adapted the surgical orthotopic transplantation model from Fumagalli *et al.* (10, 11) and implanted murine organoids, which are deficient for *Apc*, *Tp53*, *Tgfbr2*, carry a *Kras*G12D mutation and an activated/myristoylated isoform of AKT1 (hereafter termed APTKA) (16, 17) under the subserosa of the cecum of immunocompetent C57BL/6J mice (**Figure S1A-C and Movie S1**)*.* Invasive primary tumour growth as well as hepatic and peritoneal spread was monitored by video-guided laparoscopy (**Figure 1A and Movie S2**) and peritoneal tumour load was quantified using an adapted peritoneal carcinomatosis index (PCI) scoring system (**Figure S1D-E**). Upon animal sacrifice, primary CRC (PT) growth rate was 98 %. Hepatic (LM) and pulmonary metastasis (PM) rates were 67% and 8%, respectively. Lymph node metastases (LN) occured in 74% of all cases. Ultimately, a high percentage of animals (67 %) developed PC (**Figure 1B**). Gene expression profiling indicated that the PT tissue resembled human mesenchymal CRC (CMS4) (**Figure S1F**) which is shown to frequently metastasize to the peritoneal cavity when being compared to other CMSs (13, 18). To elucidate the cellular landscape of multivisceral CRC, we analysed 8,094 cells (**Figure S1G-H**) from whole-tumour samples of PT, LM and PC by droplet-based scRNA-seq. We used unsupervised clustering and two-dimensional embedding using uniform manifold approximation and projection (UMAP) as well as a marker-based annotation strategy to identify six major cell types: tumour cells (*Epcam*$^+$), B cells (*Cd79a*$^+$), T cells (*Cd3d*$^+$),

myeloid cells (*Itgam*$^+$), cancer associated fibroblasts (CAFs) (*Dcn*$^+$) and endothelial cells (*Pecam1*$^+$) **(Figure 1C-D)**. Interestingly, cellular compositions of metastatic tissues (LM and PC) differed substantially from PT: Quantification of populations in the TME revealed a differing immunological TME in both metastatic CRC tissues with increased myeloid cell populations in LM and PC as well as an obvious decrease of B cell and T cell counts in LM and a nearly complete exclusion of both immune cell populations in PC. Meanwhile, CAFs were most strongly represented in PC and increased endothelial cell populations were found in both metastatic sites with the highest abundance in LM tissue (**Figure 1C, Figure S1H**). CD45 and PDGFRB immunhistochemistry (IHC) further confirmed the reduction of immune cell infiltration in metastatic tissue and the reciprocal stromal increase in PC (**Figure S1I**). Concerning the epithelial compartment, we further identified four epithelial subpopulations in 5,533 tumour cells: cancer stem cells (CSC, *Lgr5*$^+$ and *Prom1*$^+$) and cycling progenitor cells (CP, *Prom1*$^+$ and *Ccnd1*$^+$), summarized as STEM compartment, since CP still expressed stem cell marker genes. A highly proliferative cellular compartment was annotated as transient amplifying cells (TA, *Mki67*$^+$). Finally, differentiated cells (DIFF) showed high expression of *Krt20* (**Figure 1E upper panel, F**). Of note, the distribution pattern of these epithelial subpopulations was tumour location-specific: while the DIFF population was the largest population in PT, the proliferating TA populations dominated in both metastatic sites. Most strikingly, we found a massive deregulation of the CSC compartment upon CRC metastasis: while being reduced to ~1/3 in LM compared to PT, the CSC population was increased more than 2-fold in PC (**Figure 1E, lower panel**). Based on this observation, we questioned whether the epithelial CMS (intrinsic CMS / iCMS) based on the framework established by Joanito *et al.* (19), was

location-dependent in our multivisceral CRC model. Thus, we formulated gene scores for iCMS2 (327 genes; "iCMS2 score up") and iCMS3 (67 genes; "iCMS3 score up") and observed distinct patterns of gene score expression across all three locations. Specifically, iCMS2-associated genes displayed enhanced expression in PT and PC, while iCMS3-associated transcripts exhibited upregulation within the LM epithelial compartment. Consequently, we have designated the PT and PC epithelium as iCMS2, whereas the LM epithelium has been categorized as iCMS3, emphasizing the niche-specific reprogramming of the epithelium during metastasis (**Figure S1G**). To further understand the mechanism of the potent STEM niche especially during metastasis, we analysed the metabolic scores of the STEM compartment at each site. Strikingly, VISION-based single cell metabolic analysis revealed a distinct phenotype of especially LM and PC STEM cells: While STEM cells in PT partially obtained scores for "Fatty Acid Degradation", "Glycolysis/ Gluconeogenesis" and predominantly "Oxidative Phosphorylation" (OXPHOS), the respective cellular compartment in metastases was metabolically reprogrammed in a distinct manner. While LM STEM showed the highest scores for "Glycolysis / Gluconeogenesis", PC STEM was characterized by high metabolic scores of "Fatty Acid Degradation" (**Figure 2A**). In line with this, analysis of representative genes for each metabolic pathway showed equivalent differential location-dependent expression (**Figure 2B**). To further substantiate this metabolic deregulation in the STEM compartment, we purified epithelial cells from all three sites and confirmed location-specific deregulations of metabolic patterns of glycolysis and fatty acid metabolism on protein level in the epithelium: Epithelial cells from LM show elevated levels of proteins involved in glycolytic activity, while key enzymes of fatty acid

metabolism were overexpressed in PC tumour cells (**Figure 2C**). Importantly, lipid metabolism is already known to be associated with CSC maintenance (20). To infer a potential successive niche which promotes the intercellular and CSC-specific crosstalk in the epithelial niche, we computed cell-cell-interactions using a ligand-receptor (L-R) dependent algorithm (21). Consistently, we found increased outgoing signalling from the CSC compartment towards all epithelial subtypes in PC (**Figure 2D**). Signalling pathway analyses of respective L-R-pairs showed increased outgoing Collagen, Osteopontin (SPP1), Fibronectin and Thrombospondin signalling from CSCs in PC (**Figure 2E, Figure S2A-B**), which are already known to be associated with dedifferentiation, stem cell support and metastasis (22-27). Collectively, our data demonstrate an inter-site heterogenic reorganisation of the cellular composition at respective PT and metastases sites. Additionally, we were able to decipher a site-specific iCMS of tumour epithelium and metabolic reprogramming of the stem cell compartment, leading to a self-supportive feed-forward niche in the epithelial compartment of treatment-naïve murine PC. These data implied a site-specific environmental adaption during multivisceral metastasis of mesenchymal CRC.

Inter-metastatic differences in stromal cell dynamics during CRC metastasis

CAF polarisation to an inflammatory phenotype (iCAF) in the TME of CRC is already known to be prognostically relevant, to drive therapy resistance and metastasis by supporting immune evasion and to promote invasive capacity of tumour cells (16, 28-30). We further subclustered CAFs in our murine dataset into two clusters (**Figure S3A**). Gene set enrichment analysis (GSEA) indicated upregulation of genes involved in inflammatory

pathways in cluster 2 in comparison to cluster 1. Accordingly, cells in cluster 2 were classified as iCAFs, cells in cluster 1 were termed "myofibroblasts" (myCAF) (**Figure 3A**). Site-specific quantification of respective cell populations revealed predominant existence of iCAFs in PC (**Figure 3B**). Reciprocally to the upregulation of iCAF gene expression, we found decreased expression of genes characterising antigen presenting CAFs (apCAFs) in PC (**Figure 3C**) which are reported to be involved in homing and activation of immune cells in the TME of solid tumours (31, 32), e.g. *H2-Ab1*, *H2-Aa* and *Cd74* (**Figure 3D**). Accordingly, we have already shown that B cell and T cell populations were strongly reduced in murine PC (**Figure 1C, lower panel**).

To understand the site-specific heterogeneity of a CAF-specific intercellular communication especially in metastatic CRC, we inferred communication probabilities between CAFs and tumour cells in LM and PC. Of note, we found increased numbers of putative interactions between both cell populations in PC and identified CAFs in PC as predominant sender population (**Figure 3E**). We then identified increased expression of genes like e.g. *Thbs4*, *Ptn*, *Mdk*, *Angptl4*, *Tnc*, *Col6a1*, *Col6a2*, *Thbs2*, *Lamc* and *Lamb* in CAFs from PC (**Figure 3F**). Differential coexpression analyses showed overexpression of respective L-R pairs between CAFs and tumour cells in PC, suggesting increased cell-cell communication (**Figure 3G, Figure S3B**). L-R pairs like e.g. *Lamb1/Cd44* are already known to drive the metastatic capacity of CRC and to support intratumoural CSC function by upregulation of stem cell supporting pathways (33, 34). Considering this site-specific reprogramming of CAFs in accordance with the elevated numbers of CSCs in PC (**Figure 3D**), we further analysed the differentially expressed genes between CSCs from PC and LM to understand a potential CAF-mediated transcriptomic reprogramming of this specific

epithelial cell population. Unbiased GSEA revealed significant upregulation of KEGG GO terms associated with stem cell support like Wnt and Hippo signalling (**Figure S3C**). These data suggest that CAFs in PC support the epithelial niche by directly supporting CSC survival. Furthermore, endothelial cells of the tumour stroma are already used as therapeutic targets (35). To understand the site-specific function in metastatic CRC, metastatic endothelial cells were conducted to GSEA which confirmed an inflammatory phenotype in PC endothelium compared to LM (**Figure 3H**). Accordingly, differential expression analysis showed increased expression of genes like e.g. *Lamb1*, *Itpr1*, *Hras*, *Fn1*, *Lamc1*, *Akt1*, *Nras* and *Nfkbia* in PC (**Figure 3I**). Accordingly with the observed upregulation of genes involved in inflammation and proliferation, we set up gene scores for antigen presentation and angiogenesis with established gene panels (**Table S4**). Interestingly, we obtained a loss of antigen presentation capacity paired with an increased angiogenic function in PC endothelium (**Figure 3J**), suggesting a locoregional attenuated immune stimulation and increased neovascularisation supporting the outgrowth of PC.

Taken together, our data show a distinct and PC-specific reprogramming of the metastatic stromal cells. We show increased support of the locoregional CSC niche by CAFs as well as enhanced immunosuppressive inflammation and angiogenic activity of endothelial cells.

Location-specific anti-tumoural immunity during CRC disease progression

Having shown reduction of immune cells of adaptive immunity during metastasis to the peritoneal cavity, we aimed to describe the innate immune cell compartment in multivisceral CRC. Whereas myeloid cells in CRLM are already investigated (6), the role

of myeloid cells in PC is still lacking. Therefore, we analysed *Itgam*$^+$ myeloid cells from PT, LM and PC (**Figure S4A**). Quantification of subtypes revealed a decrease of potentially anti-tumoural conventional dendritic cells (cDCs) during disease progression with a concomitant increase of proliferative (*Mki67*$^+$) macrophages. Inflamed tissue macrophages and neutrophils could only be identified in LM. Moreover, we analysed the location-dependent reprogramming of *Mrc1*$^+$ macrophages and found concordant polarization with already published data (6). In metastases, *Mrc1*$^+$ macrophages exhibited upregulation of genes involved in M2 polarization and immunosuppression like *Lipa*, *Marco* and *Id3*, while *Mrc1*$^+$ macrophages from PT expressed higher levels of inflammatory cytokines like e.g. *Tnf*, *Ccl3*, *Ccl4*, *Il23a*, and *Cxcl1* (**Figure S4B**).

Since whole tumour data showed a massive decrease of B and T cells during metastasis (LM and PC) (**Figure 1C**), we purified CD45$^+$ CD11b$^-$ infiltrative cells from all three sites by fluorescence activated cell sorting (FACS) (**Figure S4C**) to enable analysis of the adaptive compartments. Here, we analysed 15,714 *Cd79a*$^+$ B cells, *Cd3d*$^+$ T cells, *Klrb1*$^+$ NK (Natural killer) cells and *Kit*$^+$ mast cells by scRNA-seq after quality control (**Figure S4D-E**). Annotation of cells was performed by a marker-based strategy (**Figure S4F, Figure 4A**). Quantification of cell types revealed low abundance of mast cells with a predominant existence in PT, while we obtained approximatively equal location dependent compartment sizes for B and T cells, as well as a predominance of NK cells in LM (**Figure 4A**). Analysing these immune cell clusters in detail, T cells contained multiple clusters representing the transition from naïve to effector CD4$^+$, CD8$^+$ and γδ T cells with the latter decreased in LM (**Figure S4G**). Further subcluster analyses from T cells marked increased infiltration of naïve CD8$^+$ T cells, exhausted CD8$^+$ T cells, *Foxp3*$^+$

regulatory T cells (Treg) and cytotoxic CD8$^+$ T cells during metastasis (**Figure 4B**). To molecularly understand a potential functional reprogramming of T and NK cell subtypes, we performed VISION based metabolic scoring on the T and NK cell populations. OXPHOS can be associated with terminal T cell exhaustion and dysfunction in cancer (36-38), while it metabolically fosters anti-tumoural NKT cell and NK cell activity (39, 40). Accordingly, highest baseline OXPHOS scores were witnessed in exhausted CD8$^+$ T cells (**Figure S4H**) and location dependent analysis of OXPHOS activity revealed increased scoring in T and NK cells of both metastatic locations compared to PT (**Figure 4C**). Additionally, this metabolic conversion was also obtained in metastatic T cells on a subtype level (**Figure S4I**). While the number of potentially anti-tumoural adaptive immune cells like cytotoxic CD8$^+$ T cells increased in metastases, we found upregulation of markers for T cell exhaustion and downregulation of markers for T cell activation in PC (**Figure 4D**). This observation was in accordance with elevated OXPHOS genes in PC. Furthermore, we also analysed markers for degranulation in NK cells, since we observed elevated numbers of this population in metastases. Interestingly, the degranulation markers *Gzmb* and *Prf1* were expressed in a higher manner in metastases, suggesting increased cytotoxicity (**Figure 4E**). These data depict a dysfunctional phenotype and metabolic reprogramming of adaptive anti-tumoural immune cells in LM and PC as well as an increased cytotoxic function of infiltrative NK cells in respective lesions.

Impairment of B cell networks and altered adaptive immunity in metastasized CRC.

Precondition for adequate adaptive cytotoxicity is a subtle concerted interplay of T and immunoregulatory B cells which participate in antibody production and antigen

presentation (41-43). To analyse B cell functionality and T and B cell interactions in the distinct locations, we further subclustered 3,355 B cells and identified seven B cell subtypes incorporating different developmental stages: Immature *Cd24a*⁺ B cells, *Irf4*⁺ B cells and naïve *Ccr7*⁺ B cells and marked populations during stages of B cell maturation or without priming via antigens. Memory B cells, IgM⁺ Plasma cells, IgG⁺ Plasma cells and *Cd38*⁺ IgG⁺ Plasma cells typified B cell subtypes which already were primed upon antigen recognition. (**Figure 5A upper panel**, **Figure S5A**). We found unequal distribution of B cell subtypes in primary and metastases: While primed B cell subtypes were predominantly occurring in PT, most immature and naïve subtypes were found in LM and PC (**Figure 5A lower panel**). To decipher the potential antigen presenting function of B cells, we analysed differential L-R signalling interactions in B and T cell populations and found B - T cell as well as inter-T-cell interactions as expected (**Figure S5B**). To compare the outgoing B cell signalling between PT and metastatic tissue, LM and PC samples were pooled and termed as "MET". Strikingly, we obtained a reduction of outgoing B cell signalling in all MET B cell subtypes when being compared to PT B cells, suggesting an altered B cell function specifically in metastases (**Figure 5B**). Summarized differential pathway analysis confirmed downregulation of MHC-II signalling pathways in MET B and T cells, implicating a reduction of MHC-II dependent antigen presentation, accompanied by increased PD-L1 pathway activation (**Figure 5C**). We assumed a reduction of the canonical MHC-II dependent Th1 CD4⁺ T cell interaction and could show a drastic loss of MHC-II-driven L-R pairs between B and Th1 CD4⁺ T cells in MET (**Figure 5D**). Additionally, we found increased mRNA expression of *Cd274*

(encoding for PD-L1) in MET Th2 CD4⁺ T cells, which could indicate a worsened immunosuppressive phenotype of T cells in metastases (**Figure S5C**).

To further uncover inter-metastatic differences in the intercellular regulation of effector T cell function, we also analysed differential signalling sender capacities of B and T cells between LM and PC (**Figure 6A**). Here, we identified Th1 CD4⁺ T cells as prominent sender cells, especially towards cytotoxic and exhausted CD8⁺ T cells (**Figure 6B**) with increased sender capacities in PC (**Figure 6C**). PD-L1 signalling was significantly upregulated in the summarized communication pathway analysis in PC (**Figure S6A**) and Th1 CD4⁺ T cells from PC expressed higher mRNA levels of *Cd274* (**Figure 6D**). Consequently, further differential Th1 Cd4⁺ T cell dependent PD-L1 signalling analysis showed a PC-specific increase of PD-L1 dependent signalling towards effector T cells (**Figure S6B**). Taken together, these data imply a potentially disrupted antigen presenting function of B cells represented by a loss of MHC-II dependent L-R signalling in metastatases towards T cells. Furthermore, we demonstrate a location-specific PD-L1 dominant Th1 CD4⁺ T cell phenotype, with increased PD-L1 L-R interaction towards cytotoxic CD8⁺ T cells in PC. These results underline the establishment of site-specific TMEs with altered adaptive immune responses.

Murine multivisceral APTKA CRC mimics human stage IV CRC

We next tested whether murine multivisceral APTKA CRC mimics human UICC *(*Union for International Cancer Control) IV CRC. In order to analyse transcriptomic similarities, we used published mRNA-Seq data from human patient-matched primary tumours (hPT) and peritoneal carcinomatosis (hPC) (44) as well as hPT and liver metastases (hLM)

(GSE50760) and integrated these data with our murine mRNA-Seq data we obtained from three primary tumours (mPT), four liver metastases (mLM) and three peritoneal carcinomatosis (mPC) samples (**Figure 7A**). Principal component analysis (PCA) of the mouse data showed localisation dependent clustering, acknowledging the inter-site-specific differences in the scRNA-seq data (**Figure S7A**). To eliminate species-specific differences, we performed batch corrected PCA and found tumour site-specific clustering of mPT and hPT as well as mLM and hLM (**Figure 7B**). Next, we compared the immunological TME of murine and human LM, by applying the Microenvironment Cell Populations-counter (MCP-counter) deconvolution algorithm (45). Here, we found equivalent proportions of macrophages, B cells, NK cells, and T cells and similar cytotoxicity scores in murine and human LM (**Figure 7C**). Importantly, strong accordance between human and murine PT and PC was also obtained for the PCA and MCP-counter analysis (**Figure 7D-E).** Differential expression analyses revealed 443 overlapping DRGs between PT and PC from human and murine background (**Figure S7B**). GSEA in murine tissues indicated upregulation of genes involved in "EMT" in PC (**Figure 8A**). Consistently, we also found enrichment of genes involved in "EMT" in hPC (CRS) (**Figure 8B**) and could show upregulation of *Snai2* / *Slug* downstream target genes in human and murine PC (**Figure S8A**). Accordingly, we found relevant increase in protein expression of EMT proteins like ZEB1, N-cadherin, α-SMA, Vimentin, LOX, COL1A1 in murine and human PC (**Figure 8C-D**). To further understand the cellular origin of this increased EMT marker expression, we conducted IHC for EPCAM to stain tumour epithelium, as well as VIM and ZEB1 in murine and human samples. In accordance with our results from the scRNASeq analysis, we found a strong dominance of the stromal compartment,

visualized by a reduction of EPCAM⁺ tumour cells in PC (**Figure 8E**). Furthermore, VIM, as well as ZEB1 expression was not found in the epithelium, but the stromal compartment (**Figure 8E**). Quantification of VIM⁺ and ZEB1⁺ cells per HPF revealed a marked increase for both markers in murine and human PC (**Figure S8B**). Consequently, the mesenchymal phenotype of PC CRC underlies the increased stromal infiltration. Additionally, the fibrotic phenotype of specifically PC in mouse and human CRC, was corroborated by COL1A1 IHC and Masson Goldner stainings (**Figure S8C**). To gain further insights into whether our murine multivisceral APTKA CRC model also recapitulated human stage IV CRC in terms of cellular composition and TME, we performed scRNA-Seq from human biopsies of three primary CRC, four LM and four PC tissues. This analysis revealed broadly similar clusters and location-dependent compositions as the murine model (**Figure S8D**). Consistent with proportions obtained from the murine model, PC samples were largely depleted of B cells (**Figure S8E**). We next wanted to ascertain that mouse and human cell types are fully comparable in the TME. When integrating both human and mouse PT/CRC, LM and PC following conversion of mouse genes to their human orthologues, all main cell types and locations clustered together independently of the species of origin (**Figure S8F**). Accordingly, cell proportions of the combined data further validated the loss of B-cells in human and mouse PC, eliminating any potential clustering artefacts (**Figure S8G**). Thus, our results delineate a high similarity of murine LM and PC with human LM and PC and a stroma dominant mesenchymal phenotype of murine and human PC, emphasizing the high translational potential of the APTKA multivisceral CRC mouse model for further molecular

site-specific deconvolution of CRC metastasis and future preclinical evaluation of therapeutic approaches.

Intraperitoneal application of checkpoint inhibitors reconstitutes effector T cell function in PC and emphasizes the importance of developing site-specific CRC therapy

So far, immune checkpoint blockade (ICB) in hepatic metastasis is only shown to be effective in MSI-high (microsatellite instability high) CRC (46, 47). Based on our results, anti-PD1 therapy should specifically be evaluated in peritoneal CRC metastasis of non-MSI CRC. To demonstrate the translational potential of the APTKA orthotopic mouse model and to verify our presented data we tested the site-specific reactivation of CD8$^+$ T cells by administration of anti-PD1 therapy. Stage IV CRC was established as described before (**Figure 1A-B, Figure S1A-C**). On day 37 and 44, we intraperitoneally treated mice with 300µg anti-PD1 antibody. Control animals were treated by equivalent IgG isotype control (**Figure 9A**). Animals were sacrificed on day 56 and PT, LM and PC tissue were harvested. Function of infiltrative CD8$^+$ effector T cells were analysed using FACS. Importantly, we found substantial reduction of PD1 expression and increased degranulation markers IFNγ and PRF1 upon ICB specifically in PC tissue, which indicated compartment and location dependent therapy response, since CD8$^+$ T cells in PT and LM were not substantial activated by ICB (**Figure 9B**). Furthermore, anti-PD1 application tended to result in increased numbers of infiltrative CD8$^+$ T cells and in upregulation of granzyme B and CD107α in PC without statistical significance (**Figure S9A**). In accordance with these results, macroscopic PC load could markedly be reduced by ICB

(**Figure S9B**). Specific cell death induction of the epithelial compartment of respective tumour site was then evaluated using FACS. Importantly, we found marked upregulation of cell death in the tumour cell compartment of PC upon anti-PD1 administration, whereas tumour cells of PT and LM were not affected (**Figure 9C**). To further investigate the spatial reconstitution of the immunological TME by ICB, we performed IHC for B and cytotoxic T cell infiltration (b220 and CD8). Intriguingly, our findings reveal an enhanced infiltration of CD8$^+$ T cells specifically within the PC lesions following anti-PD1 treatment in the tumour center (CT) as well as the invasive margin (IM) while this alteration was not observed in PT and LM (**Figure 9D-E**). Quantification of b220 revealed an increase of B cell infiltration especially at the invasive margins of PC mass, suggesting a potential restauration of B cell dependent antigen presentation (**Figure 9D, F**). These data are in accordance with our scRNA-seq results, where we have suggested CD8$^+$ T cells in PC as location-specific targets for immunomodulation. Hence, our results depict the importance of a further location-specific understanding of CRC metastasis for the development of individualized and location-adapted therapeutic approaches.

Discussion

To date, single-cell transcriptome studies in CRC have either focused on specific tumour cell populations or on the comparison of two tumour sites (6, 48). In this study, we comprehensively mapped the location dependent cellular landscape of multilocular CRC in an orthotopic, organoid-driven mouse model, which mimics human UICC IV disease with peritoneal and liver metastases. This approach enabled us to decipher intercellular communication networks and metabolic changes during metastasis to different locations. We were able to not only characterise lineage dependent transformations in tumour cells, but also in low-abundant TME populations like stromal and immune cells without the influence of therapeutic interventions.

Specifically, we demonstrated the dominance of CSCs in PC, preserving a self-promoting niche by stem cell supportive intercellular L-R signalling and increased fatty acid metabolism. This was consistent with previous studies which have demonstrated a crucial role of fatty acid metabolism for stemness, maintenance, self-renewal and therapy resistance of CSCs (20, 49-51). Additionally, this niche is supported by CAFs, potentially leading to increased Wnt- and Hippo signalling in respective CSCs. In our model, CAFs and endothelial cells also seem to drive the inflammatory and immune suppressive phenotype of PC, accompanied by dysfunction of the immunological TME. Our insights into the stromal compartment correspond with published studies, where multiple subtypes of CAFs have been identified in different cancer entities (31, 32, 52-56).

In the metastatic TME, adaptive anti-tumoural immune cells like cytotoxic CD8^{+} T cells lose their cytolytic activity and become exhausted, accompanied by upregulation of OXPHOS metabolism. Simultaneously, further cytotoxic cells like NK cells gain activity in

LM and PC. Metabolic reprogramming towards OXPHOS and simultaneous activation of NK cells has already been studied in variable diseases (57-59).

Furthermore, we distinguished inter-metastatic Th1 CD4$^+$ T cell function, which in PC is predominantly governed by immunosuppressive PD-L1 signalling towards CD8$^+$ cells and accompanied by a loss of B cell-dependent MHC-II signalling, potentially resembling a disturbed antigen presenting function of MHC-II$^+$ B cells in PC. In a translational approach, we demonstrated strong location-dependent concordance of the orthotopic mouse model with human multilocular CRC metastasis. Our bulk proteomic and transcriptomic analyses suggest congruent deconvolution of the configuration of murine and human LM (60) and PC (44) from both species. Concomitantly, murine and human PC are characterized by increased EMT marker expression originating from a strong stromal infiltration at respective site. Hence, our data depict explicit site-specific adaptations to local environments during disease progression in the reported mouse model mimicking human multivisceral CRC.

Most of the published stage IV CRC mouse models rely on direct intraperitoneal or intrasplenic injections of permanent tumour cell lines into immunocompetent or immunodeficient mice which do not mimic the physiological route of metastasis (61). Furthermore, permanent cell lines are selected epithelial subpopulations of the original tumour tissue. Therefore, they do not resemble the mutational burden and architecture of the original tumour. In contrast, tumour organoids recapitulate the molecular and architectural features of the original tumour both of mice and men (62, 63). In our model, CRC cells from invasive primary tumour tissue spread hematogenously and *per continuitatem* and thereby lead to multivisceral metastatic disease.

In our study, adapted from Fumagalli *et al.* (10, 11), APTKA organoids were surgically implanted into the subserosa of the cecum of immunocompetent mice. Infiltrative direction is inverted when being compared to the physiological condition of CRC tumourigenesis. Consequently, the process of peritoneal metastasis represents a relatively smaller barrier to traverse when compared to human CRC, where tumour cells must navigate across the basal membrane, the muscular and the serosal layer to access the peritoneal space which could be one explanation for the high percentage of PC obtained in our model. Importantly, we can depict a transluminal epithelial barrier breach already at day seven after implantation of the organoids. Consequently, tumour cells -for the most time of the experiment- are already also reinfiltrating from the luminal side towards the colon wall and therefore are exposed to intestinal stimuli similar to human CRC. The mutational spectrum of the APTKA organoids used in this project can also be found in human CRC but accumulation of the whole mutational spectrum is not being observed in the majority of CRC patients (CMS4, ~ ¼ of CRC patients). Still, we could show a strong overlap of murine and human tumour tissue in two large patient cohorts of bulkRNA-seq analyses, regardless of the mutational burden of the human CRC samples. In our stage IV CRC model, orthotopic APTKA implantation is being performed into the right-sided colon. Here, we make use of the exclusion of the caecal blind loop from the lower gastrointestinal passage. This facilitates longer experimental timeframes until successful metastatic disease occurs without intestinal obstruction by the PT.

Importantly, based on the collected data in this project, we also propose a PC-specific therapeutic approach. In a proof-of-concept experiment, we successfully treated murine APTKA PC CRC by intraperitoneal application of anti-PD1 biologicals. This led to

reactivation of exhausted CD8^{+} T cells and increased tumour cell death in intraperitoneal tumours. Macroscopic quantification of tumour mass revealed a successful reduction of intraperitoneal tumour load upon ICB.

Our observations reinforce the necessity for a highly location-specific evaluation of therapeutic interventions, since e.g. intraperitoneal and systemic application of chemotherapy show very limited efficacy in PC. To our knowledge, immunomodulatory drugs like e.g. systemic application of ICB have only been investigated for the treatment of CRLM (64, 65) yet. Here, ICB only was successful in MSI-high tumours and thereby is reserved for a small percentage of patients. It needs further preclinical investigations to elucidate, if locoregional intraperitoneal ICB in combination with e.g. established treatment protocols or novel immunotherapeutics is a promising therapeutic approach in PC patients.

In summary, we present the comprehensive cellular and molecular landscape of multivisceral CRC and illustrate specific location dependent reconfiguration of tumour cells and TME. Our findings provide insights into the complex and multifaceted process of metastatic adaptations to local environments and identified exhausted effector CD8^{+} T cells as potential PC-specific therapeutic targets.

Methods

Human tumour tissue

Tumour tissues of patients with primary CRC and metastatic LM and PC were obtained from surgical tumour resections after routine pathological analysis and were either embedded in paraffine, processed for Western Blotting or were enzymatically digested for FACS or single cell RNA sequencing with the Human Tumour Dissociation Kit (Miltenyi) according to the manufacturer's instructions.

Organoids and Organoid Culture

APTKA organoids are tumour organoids that are devoid of *Apc*, *Tp53*, *Tgfbr2* and express constitutively active *Kras* (*KrasG12D*) and an activated/myristoylated isoform of AKT1 (17). The organoids are a gift from F. Greten, Georg-Speyer-Haus, Frankfurt. APTKA tumour organoids were maintained in basal medium (Advanced DMEM-F12 supplemented with penicillin/streptomycin, HEPES 10mmol/l (Invitrogen), Glutamax 1x (Invitrogen), N2 1x (Gibco), B27 1x (Gibco), and N-Acetylcysteine 1mmol/l (Sigma)) supplemented with Hygromycin (200 µg/ml) and puromycin (2 µg/ml). The organoids were subcultured in Cultrex basement membrane extract (bio-techne) every 5-7 days.

Mice

8 - 12 week-old male and female C57BL/6J mice from Charles River, Germany or CEMT, Freiburg were used as acceptor mice for tumour organoids in the mouse model. Interventions were performed during light cycle. Animals were not specifically fasted.

Surgical Transplantation of Organoids under the subserosa of the cecum

Cultured APTKA organoids were dissociated into a single-cell suspension by mechanical disruption followed by enzymatic digestion for 20 minutes at 37°C using TrypLE (Gibco) and were washed once in ice-cold PBS. Single cells were then resuspended in an ice-cold Type I collagen/5x Collagen neutralization Buffer (4:1 (v/v) ratio) with a concentration of 200.000 cells/10 µl. The 5x Collagen neutralization buffer is composed of 2.5 g alpha MEM powder (5x) and 2 % (wt/vol) $NAHCO_3$ in 45 ml Aqua dest. and 5 ml of 1M HEPES and set to pH 7.5. 10 µl domes of collagen were plated in 6 well plates. The domes polymerize for 45 minutes at 37 °C. Afterwards basal medium (Advanced DMEM-F12 supplemented with penicillin/streptomycin, HEPES 10mmol/l (Invitrogen), Glutamax 1x (Invitrogen), N2 1x (Gibco), B27 1x (Gibco), and N-Acetylcysteine 1mmol/l (Sigma)) supplemented with 10 µM Y-27632 (Tocris Bioscience). The collagen domes were cultured overnight till transplantation. At the day of transplantation the mice were shaved and anesthetized with 2% (v/v) isoflurane. Analgesia was guaranteed by intraperitoneal injections of 100 µl 0.1 mg/kg buprenorphine. Mice were placed on their backs on a heating pad and legs were fixed. Isoflurane was lowered to 1.8 % (v/v). A 10 – 15 mm incision was made along the *linea alba* to open the abdomen. The cecum was placed on a wet sterile gauze. A 3 – 4 mm incision through the cecal serosa is made at the end of the cecum in an area without vessels. The serosa was separated from the submucosal layer and a deep pocket of about 1 cm length was performed. The pocket was enlarged to the size that the collagen dome could be deeply embedded in it. The collagen dome was placed under the serosa into the pocket and the serosa was tightly closed above the

collagen dome securing the collagen dome to be tightly embedded in its pocket. The incision in the serosa was covered with a 20 x 5 mm piece of Seprafilm (Baxter). The cecum was carefully placed back in the abdomen. The peritoneum and abdominal wall are seperately closed by a continuous suture. Before awakening, mice were subcutaneously injected with 100 µl metamizole (200 mg/kg) for ongoing analgesia. Drinking water was supplemented with metamizole (5 mg/ml) in 5 % sucrose for the following three days.

Intraperitoneal application of anti-PD1 antibody

For intraperitoneal injections of anti-PD1 antibody, InVivoMAb anti-mouse PD-1 (CD279) (#BE0146, BioXCell) was diluted to 3µg/µl in sterile PBS and 300µg were intraperitoneally injected on day 37 and day 44 after locoregional APTKA implantation. IgG2a isotype control (#BE0089, BioXCell) in the same dilution served as control.

Laparoscopy

For tumour staging of PC, laparoscopy was performed. The mice were anaesthetized as described before. The abdomen was opened by a small midline incision of 5 mm. For fixation of the endoscope the incision was surrounded by a pursestring suture. The endoscope was introduced and were fixed by the suture. Oxygen was introduced into the abdomen by the endoscope and tumourigenesis as well as metastasis was monitored.

Peritoneal carcinomatosis index (PCI)

To stage the peritoneal carcinomatosis we calculated a peritoneal carcinomatosis index similar to the human PCI index during laparoscopy. The index is calculated by measuring the amount and the size of PC in the peritoneum. We divided the peritoneum in the upper peritoneum and lower peritoneum and divide there also the left and right side and counted the amount of peritoneal metastases on the abdominal wall and the interenteric metastasis. The size was divided in small (score 1), middle (score 2) and large metastasis (score 3) or no metastasis (score 0). A small tumour is a tumour with the diameter of 0 – 2 mm, a middle sized tumour has a diameter of 2 – 4 mm and a large tumour has a diameter > 4 mm. The number of the tumours of each part of the 4 quadrants were counted and the score of each quadrant was calculated as follows score of quadrant = number of small tumours * 1 + number of middle tumours * 2 + number of large tumours * 3. The peritoneal carcinomatosis index was calculated as PCI = score of left side of the upper peritoneum + score of the right side of the upper peritoneum + score of the left side of the lower peritoneum + score of the right side of the lower peritoneum.

H&E, PAS and Masson Goldner staining

Murine and human primary tumour and CRC metastatic tissue were harvested, fixed in 4 % paraformaldehyde for 24 h and embedded in paraffine. Paraffine blocks were sliced into 3 µm thick sections. For H&E, PAS and Masson Goldner staining, slides were deparaffinized with Rotihistol (Carl Roth), rehydrated in a descending alcohol series. For H&E staining, slides were counterstained with hematoxylin (Merck) with fixation in warm tap water for 10 minutes. After hematoxylin staining slides were stained with Eosin (Sigma Aldrich). Excess Eosin is washed off with 70 % ethanol. For PAS staining, the slides were

stained with Periodic Acid Schiff (PAS) Stain Kit (Mucin Stain) (Abcam) according to the instructions. For Masson Goldner staining, the slides were stained with Masson-Goldner staining kit (Merck) according to the instructions. For all stainings, the slides were dehydrated and mounted with Rotihistokit (Roth). Slides were digitalized with Zeiss Axio Scan Z.1 Microscope Slide Scanner (Zeiss).

Immunohistology

For immunohistochemical staining, slides were deparaffinized and rehydrated. Antigen retrieval was performed by pressure cooking in 20mM Citrate Buffer (pH 6.0) or T-EDTA (pH 9.0) and the samples were incubated with 3% H_2O_2 for 30 min in order to reduce endogenous peroxidase activity. After blocking in 5% goat serum (Sigma Aldrich) for 1h, samples were incubated at 4°C overnight with primary antibodies: CD45, EPCAM, CD8, b220, PDGFRB, CD90, VIM, ZEB1, COL1A1 (see Table S2). Slides were washed and primary antibodies were detected using HRP-polymer (Zytomed Systems) according to the manufacturer's instructions. DABplus (Zytomed Systems) was added, the slides were counterstained with hematoxylin and mounted with Rotihistokit (Roth).

Western Blotting

Proteins were isolated after dissociation of whole tumour tissue with a rotor-stator homogenizer with ice-cold RIPA buffer supplemented with protease and phosphatase inhibitors (Santa Cruz and Roche). Equal amounts of protein (25 µg) were resolved in 4x Laemmli buffer (BioRad) and electrophoresed in 10 % Mini-PROTEAN TGX Precast Gels

(BioRad) and transferred to PVDF membranes (BioRad). The membranes were either blocked with 5 % non-fat dry milk or 5 % BSA in T-TBS and were incubated with primary antibodies PDHA1, LDHA, FAS, ACC1, ZEB1, VIM, CDHN, ACTA2, LOX, COL1A1, ACTB, HSP90 (1:1000 in blocking buffer, see Table S2) at 4°C overnight. After washing secondary HRP-conjugated antibodies (1:1000 in blocking buffer, Cell Signaling Technology) were incubated for 1h at room temperature. Protein expression was visualized with Immobilion Western HRP substrate (Merck Millipore).

Flow Cytometry

PT, LM and PC tissue were minced in 1-2 mm pieces and was enzymatically digested with the tumour dissociation kit mouse, Miltenyi on the gentleMACS™ Octo Dissociator according to the manufacturer's instructions. The resulting single cell suspension was filtered through a 100 μm cell strainer and erythrocytes were lysed with ACK lysis buffer, Gibco. After cell counting the cells were either stimulated for cytokine analysis or directly proceeded with antibody staining. For stimulation the cells were stimulated with Cell Activation cocktail, Biolegend for 3 hours and additionally 2 hours together with Brefeldin A, Biolegend. For FACS analysis the cells were first stained with live/dead staining with Zombie NIR Fixable Viability kit, Biolegend and Fc receptors were blocked with Fc block, Biolegend. Afterwards the cells were incubated with fluorescent-labelled antibodies (see Table S3) for surface staining in FACS buffer (PBS, 4 % FCS, 0.05% Sodium Azide) for 20 min at 4 °C. For intracellular staining the cells were fixed in Fixation buffer (Foxp3 staining buffer, Invitrogen) for 1 hours and washed in Permeabilisation buffer for two times. The cells were stained with intracellular antibodies for 20 min at 4 °C in

Permeabilisation buffer and washed once again in Permeabilisation buffer. The analyses were performed on a BD Fortessa flow cytometer.

Tumour cell isolation

Tumour cells were isolated from single cell suspensions of whole tumour tissue with the Tumor Cell Isolation Kit (Miltenyi Biotec) according to the manufacturer protocol.

mRNA sequencing (RNA-seq)

RNA isolation from tumour tissue was performed with RNeasy MiniKit, Qiagen according to the manufacturer protocol. RNA samples were sequenced by the standard Illumina protocol to create raw sequence files (.fastq files) at Genewiz, Leipzig, Germany. Mm39 genome indexes were created using STAR 2.7.9 using --runMode genomeGenerate --sjdbOverhang 100. Fastq files were aligned to the mm39 genome using STAR 2.7.9a using --outSAMtype BAM --outSAMunmapped Within --outSAMattributes Standard. Quantification was carried out using featureCounts 1.6.2 (using -p -B -C -Q 10 --primary -s 0 as parameters. Differential analysis was carried out using DESeq2 using design~=condition and standard subsequent commands. Normalisation was performed using variance stabilisation transformation (vst). Row z-scores were computed using the following following formula: z=t(scale(t(<batchj corrected vst object>),scale=T,center=T)). Clustering was performed using the heatmap.2 function. Visual inspection of the data was performed using principal component analysis. GSEA analyses were performed using GSEA 4.1.0. Raw .fastq files can be accessed via GSE202454 (GEO/NCBI).

RNA-Seq data integration

Published human CRC data was retrieved from the SRA under accession PRJNA764756. Only primary tumour data was retained from this dataset. Human CRC data was processed as described above except that it was aligned to the hg38 genome. CMS classification was performed using MmCMS 0.1.0 using the MmCMS-A function according to developer's protocol(66). Raw counts from human and mouse raw counts were merged at the gene level by converting mouse to human gene symbols using biomaRt, retaining matching genes only. This yielded 17,843 genes available for analysis. Merged data was subsequently analysed using DESeq2 using design~=batch+condition and subsequent standard commands, where batch represented either human or mouse data. Batch correction was performed using limma::removeBatchEffect on experiment assays following variance stabilisation transformation. Bias against assigned condition was performed by swapping conditions between human and mouse data, which resulted in converse groupings for PC/CRS and PT/P samples, thereby conducive to no bias. For deconvolution and microenvironment cell population counter (MCP) analyses, the deconvolute function of the Cibersort R package was used, using "quantiseq" and "mcp_counter" on normalised DESeq2 counts. Gene set enrichment analyses were performed using GSEA.

Mouse scRNA-seq

For whole tumour samples, samples from PT, LM and PC were processed for RNA isolation, library preparation, scRNA-seq and count data generation by Singleron Biotechnologies via established protocols (Cologne, Germany). Data was obtained as raw count tables as well as .fastq files (see GEO accession). Tissue from 6 mice per location were pooled before single cell dissociation. Raw count data for all three samples was obtained as h5Seurat format.

For analyses of infiltrative lymphocytes, single-cell suspensions (also see Flow cytometry) from APTKA PT, LM and PC samples (cells from 6 mice per location were pooled before tumour cell dissociation with the tumour dissociation kit mouse, Miltenyi) were subjected to single-cell sorting using a MoFlow Astrios cell sorter. After exclusion of dead and CD45- cells, all live CD45$^+$CD11b$^-$ cells were sorted and directly processed for 10X (10X Genomics) protocols.

scRNA-seq data analysis

Data collection and analyses were performed in an unsupervised manner, but not blinded to the location of the samples.

ScRNA-seq was conducted using the Chromium Next GEM Single Cell 3' Kit version 3.1. Up to 60,000 cells were processed per reaction. The dual index protocol was performed following the manufacturer's instructions. The samples were sequenced on a NextSeq1000/2000 Illumina system using P2 reagent with 100 cycles. Libraries were diluted to be loaded at 1,200 pM. Dragen software version 3.8.4 was used for sample demultiplexing to obtain paired end reads with the unique molecular identifier (UMI) and

cell barcode information on read1 and gene sequences on read 2 of the result .fastq files. After achieving a sequencing depth of around 20,000 reads per cell, .fastq files were analysed using cellranger-6.1.2 with the Gencode mouse release M24 reference genome for read alignment. Filtered raw-count matrices were further analysed using the Seurat (v4.1.0) R package (3) for data integration and unbiased clustering of single cell transcriptomes (67). Low-quality single cell libraries with less than 250 and more than 4000 detected genes and more than 20% mitochondrial counts were excluded in whole tumour samples. Here, we analysed 10,398 cells after quality control. In addition, low-quality clusters with low numbers of detected genes and high percentages of mitochondrial genes and / or nearly exclusive ribosomal gene expression that lacked expression of biologically relevant cell type markers were removed after clustering. Consequently, data analysis was performed with 8,094 annotated high-quality cells. For sorted immune cells, the mitochondrial counts threshold was set to 10%, which lead to the analysis and annotation of 15,714 cells after quality control.

Datasets from different localisations were integrated using the IntegrateData function in Seurat. Data was centred and scales using the ScaleData function. Principal component analysis (PCA) was used for dimensionality reduction and the K-nearest neighbor (KNN) graph was constructed using the first 30 principal components (PCs). Cells were clustered using the Louvain algorithm and embedded in two- dimensional space (30 PCs) using Uniform Manifold Approximation and Projection (UMAP). Differentially expressed genes between clusters were identified using Wilcoxon Rank Sum test and clusters were assigned to cell types according to expressed marker genes and their similarity to known cell types. We merged transcriptional clusters if their average gene expression profiles

were highly correlated and if they were characterized by similar cell type-specific marker genes. Plots were generated with Seurat or custom R script using ggplot2 v3.3.5. L-R interactions were calculated and plotted using CellChat v1.1.3 as already described(21). Minimal cell count per cluster for potential cell-cell interactions was set as default. Metabolic scoring was analysed using scMetabolism v0.2.1 R-package as demonstrated before (6). For adaptation to the murine species, gene symbols in the package's .gmt files were converted to murine gene symbols using biomaRt v2.50.3.

Statistics

Data are represented as mean $\pm$ standard error of the mean (s.e.m.). Significance was calculated by two-tailed Student's t test, hypergeometric test, or Benjamini-Hochberg procedure as indicated where appropriate. Statistical significance was set to $p < 0.05$ and is represented as following: ****$p<0.0001$, ***$p<0.001$, ** $p<0.01$, * $p<0.05$. Sample sizes are indicated where appropriate.

Study approval

The human study was approved by local ethical committees and was conducted according to the Declaration of Helsinki. The study was performed in accordance with the ARRIVE guidelines.

All mice experiments were performed in accordance with local guidelines and regulations of the Government of Upper Palatine, Bavaria and Ministerium Freiburg.

Data and materials availability

All raw data values can be found in the supporting data value file. All raw data, code and materials are available from the authors upon request. Raw data is deposited under GSE202454 and GSE220507 (GEO/NCBI). A supporting data values file has been supplied as single XLS file.

References

1. Torre LA, Bray F, Siegel RL, Ferlay J, Lortet-Tieulent J, and Jemal A. Global cancer statistics, 2012. *CA Cancer J Clin.* 2015;65(2):87-108.
2. Zauber AG, Winawer SJ, O'Brien MJ, Lansdorp-Vogelaar I, van Ballegooijen M, Hankey BF, et al. Colonoscopic polypectomy and long-term prevention of colorectal-cancer deaths. *N Engl J Med.* 2012;366(8):687-96.
3. Lee JW, Stone ML, Porrett PM, Thomas SK, Komar CA, Li JH, et al. Hepatocytes direct the formation of a pro-metastatic niche in the liver. *Nature.* 2019;567(7747):249-52.
4. Zhang C, Zhang L, Xu T, Xue R, Yu L, Zhu Y, et al. Mapping the spreading routes of lymphatic metastases in human colorectal cancer. *Nat Commun.* 2020;11(1):1993.
5. Yu J, Green MD, Li S, Sun Y, Journey SN, Choi JE, et al. Liver metastasis restrains immunotherapy efficacy via macrophage-mediated T cell elimination. *Nat Med.* 2021;27(1):152-64.
6. Wu Y, Yang S, Ma J, Chen Z, Song G, Rao D, et al. Spatiotemporal Immune Landscape of Colorectal Cancer Liver Metastasis at Single-Cell Level. *Cancer Discov.* 2022;12(1):134-53.
7. Roper J, Tammela T, Cetinbas NM, Akkad A, Roghanian A, Rickelt S, et al. In vivo genome editing and organoid transplantation models of colorectal cancer and metastasis. *Nat Biotechnol.* 2017;35(6):569-76.
8. Roper J, Tammela T, Akkad A, Almeqdadi M, Santos SB, Jacks T, et al. Colonoscopy-based colorectal cancer modeling in mice with CRISPR-Cas9 genome editing and organoid transplantation. *Nat Protoc.* 2018;13(2):217-34.
9. O'Rourke KP, Loizou E, Livshits G, Schatoff EM, Baslan T, Manchado E, et al. Transplantation of engineered organoids enables rapid generation of metastatic mouse models of colorectal cancer. *Nat Biotechnol.* 2017;35(6):577-82.
10. Fumagalli A, Drost J, Suijkerbuijk SJ, van Boxtel R, de Ligt J, Offerhaus GJ, et al. Genetic dissection of colorectal cancer progression by orthotopic transplantation of engineered cancer organoids. *Proc Natl Acad Sci U S A.* 2017;114(12):E2357-E64.
11. Fumagalli A, Suijkerbuijk SJE, Begthel H, Beerling E, Oost KC, Snippert HJ, et al. A surgical orthotopic organoid transplantation approach in mice to visualize and study colorectal cancer progression. *Nat Protoc.* 2018;13(2):235-47.
12. Klaver YL, Lemmens VE, Nienhuijs SW, Luyer MD, and de Hingh IH. Peritoneal carcinomatosis of colorectal origin: Incidence, prognosis and treatment options. *World J Gastroenterol.* 2012;18(39):5489-94.
13. Lenos KJ, Bach S, Ferreira Moreno L, Ten Hoorn S, Sluiter NR, Bootsma S, et al. Molecular characterization of colorectal cancer related peritoneal metastatic disease. *Nat Commun.* 2022;13(1):4443.
14. Guinney J, Dienstmann R, Wang X, de Reynies A, Schlicker A, Soneson C, et al. The consensus molecular subtypes of colorectal cancer. *Nat Med.* 2015;21(11):1350-6.
15. Dienstmann R, Vermeulen L, Guinney J, Kopetz S, Tejpar S, and Tabernero J. Consensus molecular subtypes and the evolution of precision medicine in colorectal cancer. *Nat Rev Cancer.* 2017;17(2):79-92.

16. Nicolas AM, Pesic M, Engel E, Ziegler PK, Diefenhardt M, Kennel KB, et al. Inflammatory fibroblasts mediate resistance to neoadjuvant therapy in rectal cancer. *Cancer Cell.* 2022;40(2):168-84 e13.

17. Varga J, Nicolas A, Petrocelli V, Pesic M, Mahmoud A, Michels BE, et al. AKT-dependent NOTCH3 activation drives tumor progression in a model of mesenchymal colorectal cancer. *J Exp Med.* 2020;217(10).

18. de Sousa EMF, Colak S, Buikhuisen J, Koster J, Cameron K, de Jong JH, et al. Methylation of cancer-stem-cell-associated Wnt target genes predicts poor prognosis in colorectal cancer patients. *Cell Stem Cell.* 2011;9(5):476-85.

19. Joanito I, Wirapati P, Zhao N, Nawaz Z, Yeo G, Lee F, et al. Single-cell and bulk transcriptome sequencing identifies two epithelial tumor cell states and refines the consensus molecular classification of colorectal cancer. *Nat Genet.* 2022;54(7):963-75.

20. Brandi J, Dando I, Pozza ED, Biondani G, Jenkins R, Elliott V, et al. Proteomic analysis of pancreatic cancer stem cells: Functional role of fatty acid synthesis and mevalonate pathways. *J Proteomics.* 2017;150:310-22.

21. Jin S, Guerrero-Juarez CF, Zhang L, Chang I, Ramos R, Kuan CH, et al. Inference and analysis of cell-cell communication using CellChat. *Nat Commun.* 2021;12(1):1088.

22. He C, Sheng L, Pan D, Jiang S, Ding L, Ma X, et al. Single-Cell Transcriptomic Analysis Revealed a Critical Role of SPP1/CD44-Mediated Crosstalk Between Macrophages and Cancer Cells in Glioma. *Front Cell Dev Biol.* 2021;9:779319.

23. Nallasamy P, Nimmakayala RK, Karmakar S, Leon F, Seshacharyulu P, Lakshmanan I, et al. Pancreatic Tumor Microenvironment Factor Promotes Cancer Stemness via SPP1-CD44 Axis. *Gastroenterology.* 2021;161(6):1998-2013 e7.

24. Wu X, Cai J, Zuo Z, and Li J. Collagen facilitates the colorectal cancer stemness and metastasis through an integrin/PI3K/AKT/Snail signaling pathway. *Biomed Pharmacother.* 2019;114:108708.

25. Zhong C, Tao B, Tang F, Yang X, Peng T, You J, et al. Remodeling cancer stemness by collagen/fibronectin via the AKT and CDC42 signaling pathway crosstalk in glioma. *Theranostics.* 2021;11(4):1991-2005.

26. Wang D, Li Y, Ge H, Ghadban T, Reeh M, and Gungor C. The Extracellular Matrix: A Key Accomplice of Cancer Stem Cell Migration, Metastasis Formation, and Drug Resistance in PDAC. *Cancers (Basel).* 2022;14(16).

27. Shi Y, Sun L, Zhang R, Hu Y, Wu Y, Dong X, et al. Thrombospondin 4/integrin alpha2/HSF1 axis promotes proliferation and cancer stem-like traits of gallbladder cancer by enhancing reciprocal crosstalk between cancer-associated fibroblasts and tumor cells. *J Exp Clin Cancer Res.* 2021;40(1):14.

28. Baulida J. Epithelial-to-mesenchymal transition transcription factors in cancer-associated fibroblasts. *Mol Oncol.* 2017;11(7):847-59.

29. Franci C, Gallen M, Alameda F, Baro T, Iglesias M, Virtanen I, et al. Snail1 protein in the stroma as a new putative prognosis marker for colon tumours. *PLoS One.* 2009;4(5):e5595.

30. Xuefeng X, Hou MX, Yang ZW, Agudamu A, Wang F, Su XL, et al. Epithelial-mesenchymal transition and metastasis of colon cancer cells induced by the FAK pathway in cancer-associated fibroblasts. *J Int Med Res.* 2020;48(6):300060520931242.

31. Geng X, Chen H, Zhao L, Hu J, Yang W, Li G, et al. Cancer-Associated Fibroblast (CAF) Heterogeneity and Targeting Therapy of CAFs in Pancreatic Cancer. *Front Cell Dev Biol.* 2021;9:655152.

32. Kerdidani D, Aerakis E, Verrou KM, Angelidis I, Douka K, Maniou MA, et al. Lung tumor MHCII immunity depends on in situ antigen presentation by fibroblasts. *J Exp Med.* 2022;219(2).

33. Xia P, and Xu XY. Prognostic significance of CD44 in human colon cancer and gastric cancer: Evidence from bioinformatic analyses. *Oncotarget.* 2016;7(29):45538-46.

34. Lee H, Kim WJ, Kang HG, Jang JH, Choi IJ, Chun KH, et al. Upregulation of LAMB1 via ERK/c-Jun Axis Promotes Gastric Cancer Growth and Motility. *Int J Mol Sci.* 2021;22(2).

35. Miller KD, Nogueira L, Devasia T, Mariotto AB, Yabroff KR, Jemal A, et al. Cancer treatment and survivorship statistics, 2022. *CA Cancer J Clin.* 2022;72(5):409-36.

36. Li C, Phoon YP, Karlinsey K, Tian YF, Thapaliya S, Thongkum A, et al. A high OXPHOS CD8 T cell subset is predictive of immunotherapy resistance in melanoma patients. *J Exp Med.* 2022;219(1).

37. Patel CH, Leone RD, Horton MR, and Powell JD. Targeting metabolism to regulate immune responses in autoimmunity and cancer. *Nat Rev Drug Discov.* 2019;18(9):669-88.

38. Waldman AD, Fritz JM, and Lenardo MJ. A guide to cancer immunotherapy: from T cell basic science to clinical practice. *Nat Rev Immunol.* 2020;20(11):651-68.

39. Kumar A, Pyaram K, Yarosz EL, Hong H, Lyssiotis CA, Giri S, et al. Enhanced oxidative phosphorylation in NKT cells is essential for their survival and function. *Proc Natl Acad Sci U S A.* 2019;116(15):7439-48.

40. Littwitz-Salomon E, Moreira D, Frost JN, Choi C, Liou KT, Ahern DK, et al. Metabolic requirements of NK cells during the acute response against retroviral infection. *Nat Commun.* 2021;12(1):5376.

41. Hollern DP, Xu N, Thennavan A, Glodowski C, Garcia-Recio S, Mott KR, et al. B Cells and T Follicular Helper Cells Mediate Response to Checkpoint Inhibitors in High Mutation Burden Mouse Models of Breast Cancer. *Cell.* 2019;179(5):1191-206 e21.

42. Moynihan KD, Opel CF, Szeto GL, Tzeng A, Zhu EF, Engreitz JM, et al. Eradication of large established tumors in mice by combination immunotherapy that engages innate and adaptive immune responses. *Nat Med.* 2016;22(12):1402-10.

43. Li Q, Lao X, Pan Q, Ning N, Yet J, Xu Y, et al. Adoptive transfer of tumor reactive B cells confers host T-cell immunity and tumor regression. *Clin Cancer Res.* 2011;17(15):4987-95.

44. Hallam S, Stockton J, Bryer C, Whalley C, Pestinger V, Youssef H, et al. The transition from primary colorectal cancer to isolated peritoneal malignancy is associated with an increased tumour mutational burden. *Sci Rep.* 2020;10(1):18900.

45. Becht E, Giraldo NA, Lacroix L, Buttard B, Elarouci N, Petitprez F, et al. Estimating the population abundance of tissue-infiltrating immune and stromal cell populations using gene expression. *Genome Biol.* 2016;17(1):218.

46. Eso Y, Shimizu T, Takeda H, Takai A, and Marusawa H. Microsatellite instability and immune checkpoint inhibitors: toward precision medicine against gastrointestinal and hepatobiliary cancers. *J Gastroenterol.* 2020;55(1):15-26.

47.	Andre T, Cohen R, and Salem ME. Immune Checkpoint Blockade Therapy in Patients With Colorectal Cancer Harboring Microsatellite Instability/Mismatch Repair Deficiency in 2022. *Am Soc Clin Oncol Educ Book.* 2022;42:1-9.

48.	Lee HO, Hong Y, Etlioglu HE, Cho YB, Pomella V, Van den Bosch B, et al. Lineage-dependent gene expression programs influence the immune landscape of colorectal cancer. *Nat Genet.* 2020;52(6):594-603.

49.	Mancini R, Noto A, Pisanu ME, De Vitis C, Maugeri-Sacca M, and Ciliberto G. Metabolic features of cancer stem cells: the emerging role of lipid metabolism. *Oncogene.* 2018;37(18):2367-78.

50.	Chen CL, Uthaya Kumar DB, Punj V, Xu J, Sher L, Tahara SM, et al. NANOG Metabolically Reprograms Tumor-Initiating Stem-like Cells through Tumorigenic Changes in Oxidative Phosphorylation and Fatty Acid Metabolism. *Cell Metab.* 2016;23(1):206-19.

51.	Tirinato L, Liberale C, Di Franco S, Candeloro P, Benfante A, La Rocca R, et al. Lipid droplets: a new player in colorectal cancer stem cells unveiled by spectroscopic imaging. *Stem Cells.* 2015;33(1):35-44.

52.	Lambrechts D, Wauters E, Boeckx B, Aibar S, Nittner D, Burton O, et al. Phenotype molding of stromal cells in the lung tumor microenvironment. *Nat Med.* 2018;24(8):1277-89.

53.	Schmitt M, and Greten FR. The inflammatory pathogenesis of colorectal cancer. *Nat Rev Immunol.* 2021;21(10):653-67.

54.	Elyada E, Bolisetty M, Laise P, Flynn WF, Courtois ET, Burkhart RA, et al. Cross-Species Single-Cell Analysis of Pancreatic Ductal Adenocarcinoma Reveals Antigen-Presenting Cancer-Associated Fibroblasts. *Cancer Discov.* 2019;9(8):1102-23.

55.	Kieffer Y, Hocine HR, Gentric G, Pelon F, Bernard C, Bourachot B, et al. Single-Cell Analysis Reveals Fibroblast Clusters Linked to Immunotherapy Resistance in Cancer. *Cancer Discov.* 2020;10(9):1330-51.

56.	Li H, Courtois ET, Sengupta D, Tan Y, Chen KH, Goh JJL, et al. Reference component analysis of single-cell transcriptomes elucidates cellular heterogeneity in human colorectal tumors. *Nat Genet.* 2017;49(5):708-18.

57.	Cong J. Metabolism of Natural Killer Cells and Other Innate Lymphoid Cells. *Front Immunol.* 2020;11:1989.

58.	Assmann N, O'Brien KL, Donnelly RP, Dyck L, Zaiatz-Bittencourt V, Loftus RM, et al. Srebp-controlled glucose metabolism is essential for NK cell functional responses. *Nat Immunol.* 2017;18(11):1197-206.

59.	Donnelly RP, Loftus RM, Keating SE, Liou KT, Biron CA, Gardiner CM, et al. mTORC1-dependent metabolic reprogramming is a prerequisite for NK cell effector function. *J Immunol.* 2014;193(9):4477-84.

60.	Kim SK, Kim SY, Kim CW, Roh SA, Ha YJ, Lee JL, et al. A prognostic index based on an eleven gene signature to predict systemic recurrences in colorectal cancer. *Exp Mol Med.* 2019;51(10):1-12.

61.	Bella A, Di Trani CA, Fernandez-Sendin M, Arrizabalaga L, Cirella A, Teijeira A, et al. Mouse Models of Peritoneal Carcinomatosis to Develop Clinical Applications. *Cancers (Basel).* 2021;13(5).

62. Sato T, Stange DE, Ferrante M, Vries RG, Van Es JH, Van den Brink S, et al. Long-term expansion of epithelial organoids from human colon, adenoma, adenocarcinoma, and Barrett's epithelium. *Gastroenterology.* 2011;141(5):1762-72.

63. In JG, Foulke-Abel J, Estes MK, Zachos NC, Kovbasnjuk O, and Donowitz M. Human mini-guts: new insights into intestinal physiology and host-pathogen interactions. *Nat Rev Gastroenterol Hepatol.* 2016;13(11):633-42.

64. Almquist DR, Ahn DH, and Bekaii-Saab TS. The Role of Immune Checkpoint Inhibitors in Colorectal Adenocarcinoma. *BioDrugs.* 2020;34(3):349-62.

65. Andre T, and Cohen R. Immune checkpoint inhibitors in colorectal cancer: dream and reality. *Lancet Gastroenterol Hepatol.* 2022;7(1):4-6.

66. Amirkhah R, Gilroy K, Malla SB, Lannagan TRM, Byrne RM, Fisher NC, et al. MmCMS: mouse models' consensus molecular subtypes of colorectal cancer. *Br J Cancer.* 2023;128(7):1333-43.

67. Stuart T, Butler A, Hoffman P, Hafemeister C, Papalexi E, Mauck WM, 3rd, et al. Comprehensive Integration of Single-Cell Data. *Cell.* 2019;177(7):1888-902 e21.

A Staging laparoscopy
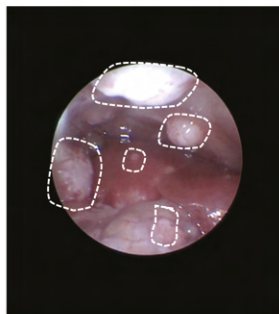
B Stage IV CRC upon orthotopic APTKA transplantation

Overview

PT

LM

PC
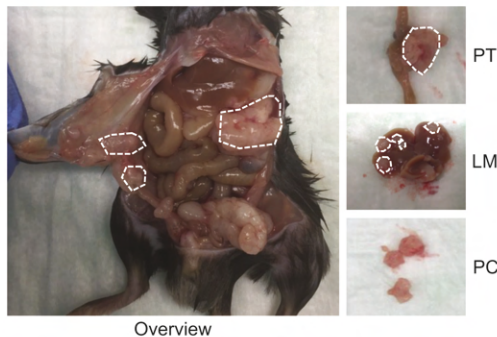
Tumor localisation upon APTKA transplantation

Localisation	% of cases
PT	98
LN	74
LM	67
PM	8
PC	67

C Whole tumour tissue - scRNA-seq

8,094 total CRC cells

CAFs
Myeloid cells
T cells
B cells
Tumour cells
Endothelial cells

UMAP2
UMAP1

- Tumour cells
- B cells
- T cells
- Myeloid cells
- CAFs
- Endothelial cells

Whole tumour mass

TME only

Cell proportions (%)
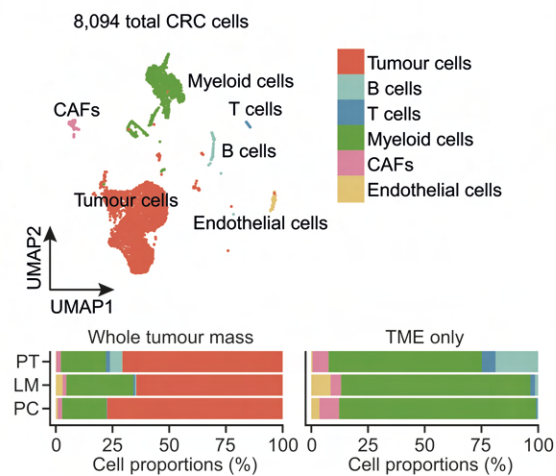
D Whole tumour tissue - celltype marker genes

Genes: Epcam, Cd79a, Cd3d, Itgam, Dcn, Pecam1

Tumour cells, B cells, T cells, Myeloid cells, CAFs, Endothelial cells

PE: 0, 25, 50, 75, 100

AE: 1.0, 0.5, 0.0, -0.5
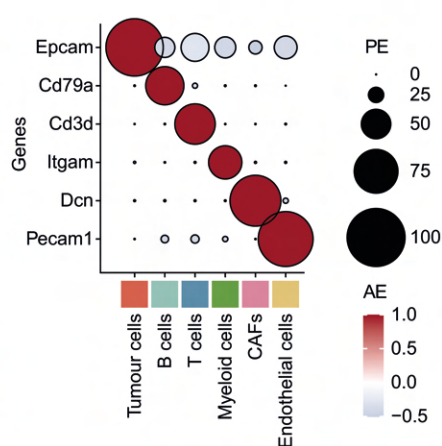
E Epithelial tumour cells - scRNA-seq

5,533 epithelial tumour cells

CSC STEM
CP
TA
DIFF

UMAP2
UMAP1

- DIFF
- TA
- CP
- CSC

PT
LM
PC

Cell proportions (%)
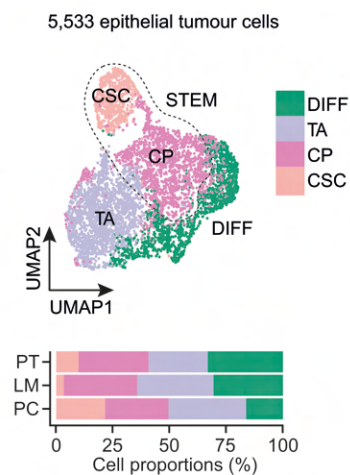
F Epithelial tumour cells - celltype marker genes

Genes: Krt20, Mki67, Ccnd1, Prom1, Lgr5

CSC, CP, TA, DIFF

PE: 0, 25, 50, 75, 100

AE: 1.0, 0.5, 0.0, -0.5
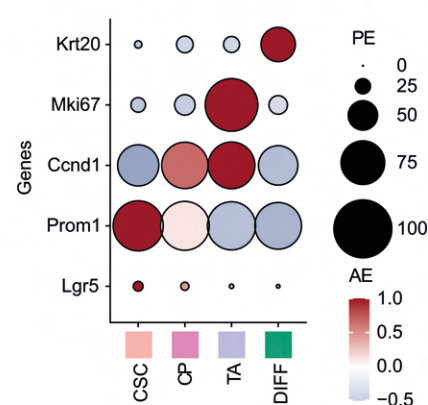
Figure 1: A distinct cellular and functional landscape of murine primary CRC, LM and PC

A. Exemplary screenshot during murine laparoscopy after eight weeks. White dashed lines mark interenteric and abdominal wall peritoneal tumours as well as liver metastases. **B.** Overview of murine metastasized stage IV CRC upon animal sacrifice (left panel). Quantification of location dependent macroscopic tumour mass in %. Locations: primary tumour (PT), lymph node metastasis (LN), liver metastasis (LM), pulmonary metastasis (PM) and peritoneal carcinomatosis (PC) (right panel). **C.** UMAP plot of 8,094 cells identified by joint application of RCA and CCA and color-coded by cell type (upper panel). Proportions of all cell types in PT, LM and PC (left lower panel) or of the TME (right lower panel) on average are shown. **D.** Canonical marker gene expression for multiple cell types centred to the average expression of each gene across all cells. The dot size represents the proportion of expressing cells in each cluster. PE: percent expressed. AE: average expression. **E.** UMAP plot of 5,533 tumour cells in the identified by joint application of RCA and CCA and color-coded by cell subtype (upper panel). Proportions of all cell types in PT, LM and PC (lower panel) on average are shown. **F.** Canonical marker gene expression for epithelial cell subtypes centred to the average expression of each gene across all cells. The dot size represents the proportion of expressing cells in each cluster. PE: percent expressed. AE: average expression.

A Organotropic metabolic reprogramming of STEM CRC cells

Scaled Values

- Fatty Acid Metabolism
- Glycolysis
- OXPHOS

PT LM PC
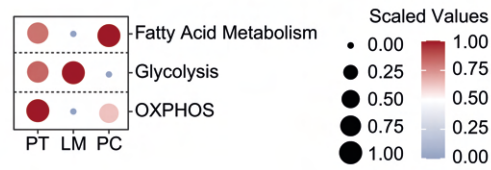
B Metabolic gene expression in STEM CRC cells

	PT	LM	PC	
Aldh2				Fatty Acid Metabolism
Adh5				
Acadl				
Tpi1				Glycolysis
Ldha				
Aldoa				
Sdhd				OXPHOS
Ndufa4				
Cox17				

PE
- 40
- 60
- 80

AE
1.0
0.5
0.0
-0.5
-1.0

(p < 0.05)
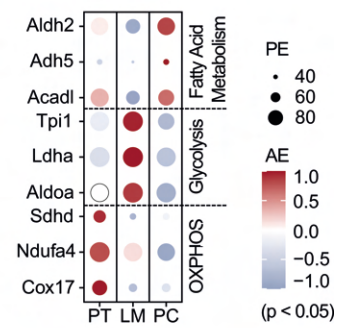
C Metabolic reprogramming of epithelial tumour cells in PT, LM and PC

kDa   PT PT LM LM PC PC

43 —   anti-PDH1
90 —   anti-HSP90   Glycolysis
37 —   anti-LDHA
90 —   anti-HSP90

273 —   anti-FAS
90 —   anti-HSP90   Fatty acid metabolism
265 —   anti-ACC1
90 —   anti-HSP90
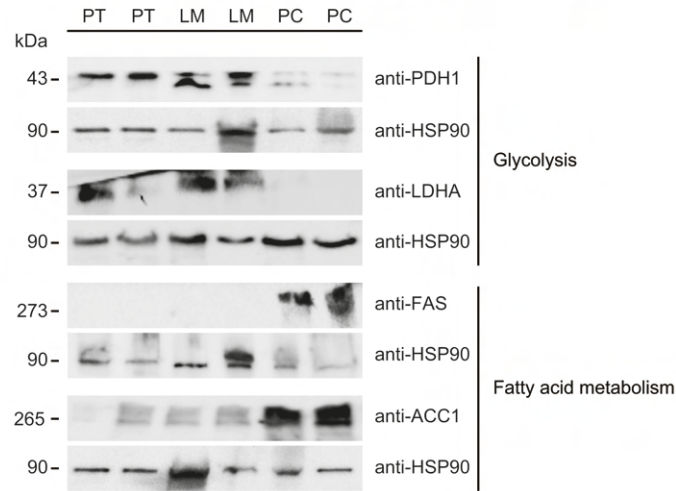
D Predominant intraepithelial CSC dependent signaling niche in PC tissue

PT   LM   PC

DIFF   DIFF   DIFF

CP   TA   CP   TA   CP   TA

CSC   CSC   CSC
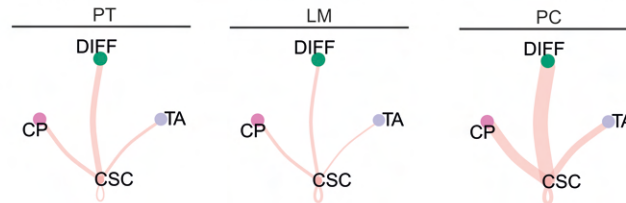
E Organotropic intraepithelial outgoing signaling
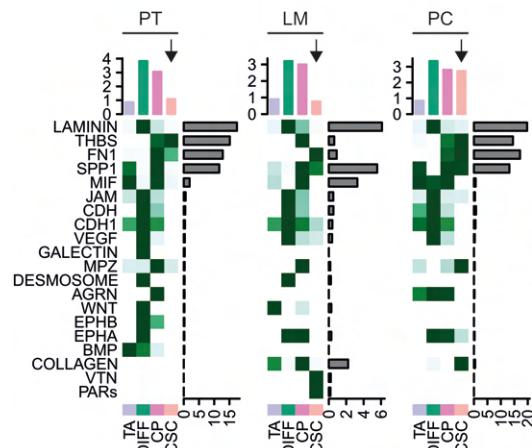
PT   LM   PC

LAMININ
THBS
FN1
SPP1
MIF
JAM
CDH
CDH1
VEGF
GALECTIN
MPZ
DESMOSOME
AGRN
WNT
EPHB
EPHA
BMP
COLLAGEN
VTN
PARs

Relative strength
1
0

TA DIFF CP CSC

Figure 2: Location-specific metabolic reprogramming of the STEM compartment in multivisceral CRC

A. Metabolic activity analysis in the STEM compartment of PT, LM and PC. Circle size and colour represent the scaled metabolic score. **B.** Expression of the top 3 differentially expressed metabolic genes in the STEM compartment of PT, LM and PC centred to the average expression of each gene across all locations. The dot size represents the proportion of expressing cells in each cluster. p<0.05. **C.** Representative Western blot showing expression of depicted proteins in pooled epithelial lysates (n=5 animals per column) from murine PT, LM and PC. Separate oading control for each Western Blot: HSP90. The experiment was performed twice. **D.** Significant ligand-receptor pairs between any pair of two epithelial cell populations in PT, LM and PC. Width represents the communication probability. **E.** Heatmap shows the relative importance in depicted signalling pathways for each cell group based on the computed centrality measures in PT, LM and PC. Arrows: Outgoing signalling patterns from CSCs.

A iCAFs have an inflammatory phenotype

#1 INFLAMED_ENDOTHELIUM
#2 GOBP_PRODUCTION_OF_MOLECULAR_MEDIATOR_
    INVOLVED_IN_INFLAMMATORY_RESPONSE
#3 GOBP_ACUTE_PHASE_RESPONSE
#4 GOBP_CYTOKINE_PRODUCTION_INVOLVED_IN_INFLAMMATORY_RESPONSE
#5 GOBP_WOUND_HEALING_INVOLVED_IN_INFLAMMATORY_RESPONSE
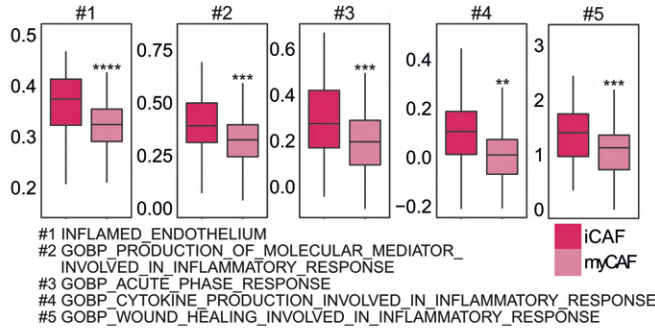
iCAF
myCAF

B iCAFs are predominant CAFs in PC

UMAP2
UMAP1

iCAF
myCAF

CAF populations

PT
LM
PC

0   25   50   75   100
Cell proportions (%)
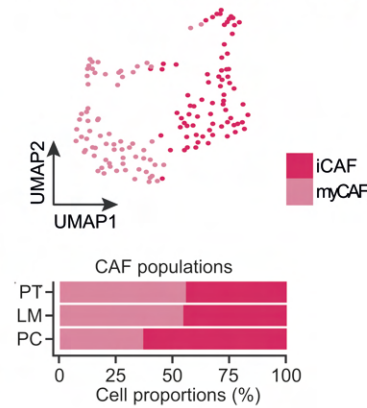
C apCAF gene score in CAFs

apCAF score Expression

****
****

CAFs PT
CAFs LM
CAFs PC
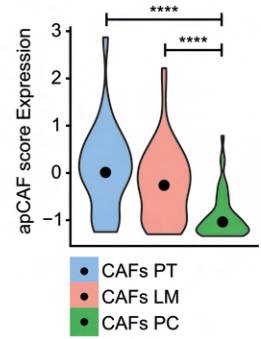
D Site specific apCAF gene expression in CAFs

Top 3 genes

H2-Ab1
H2-Aa
Cd74

CAFs_PT   CAFs_LM   CAFs_PC

% expressed
0
25
50
75
100

Average Expression
1.0
0.5
0
-0.5
-1.0
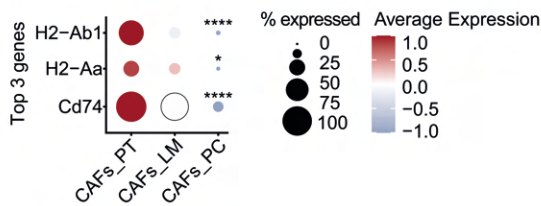
E Differential number of interactions between CAFs and tumour cells in metastatic CRC

CAFs

Tumour cells

UP in PC
DOWN in PC

(p < 0.05)

F CAF signaling in LM and PC

Expression Level

Thbs4   ****
Ptn   ****
Mdk   **
Angptl4 **
Tnc   ****
Col6a1 ***
Col6a2
Thbs2   ***
Lamc1   ***
Lamb1   **
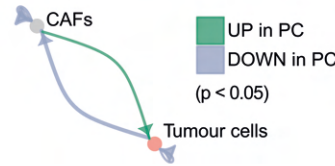
CAFs LM
CAFs PC
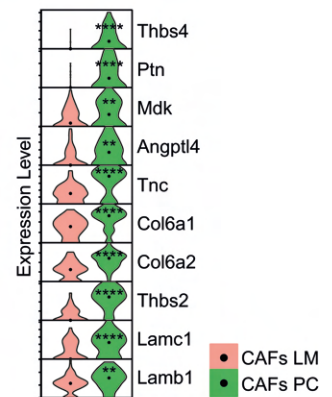
G Significantly upregulated CAF signaling in PC tissue compared to LM

CAFs
Tumour cells

(p < 0.05)
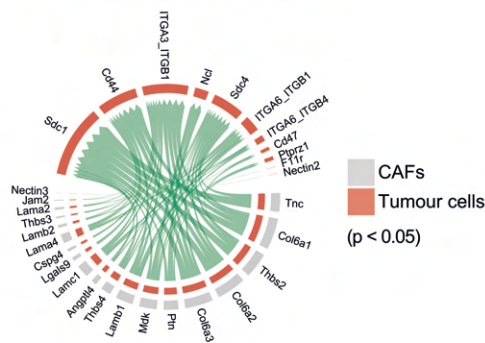
H Inflammatory phenotype of metastatic endothelium in PC

Pathway Enrichment

#1   *
#2   ***
#3   *

LM
PC

#1 - WP_INFLAMMATORY_RESPONSE_PATHWAY
#2 - GSE6092_UNSTIM_VS_IFNG_STIM_ENDOTHELIAL_CELL_UP
#3 - WP_RESISTIN_AS_A_REGULATOR_OF_INFLAMMATION
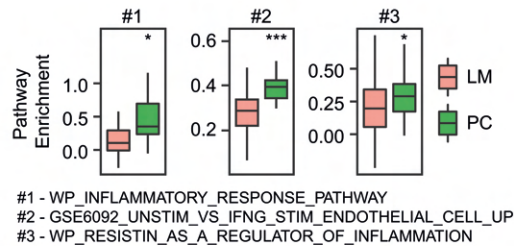
I Endothelial signaling in LM and PC

Expression Level

Nfkbia **
Nras   *
Akt1   **
Lamc1   ****
Fn1   ****
Hras   **
Itpr1
Lamb1   ****

LM   PC
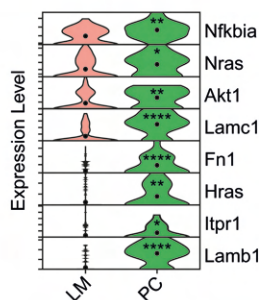
J Immunosuppresive and proliferative phenotype of PC endothelium

Antigen presentation   Angiogenesis

****   ****

LM
PC

Expression Level
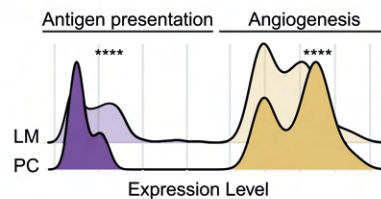
Figure 3: Inter-metastatic differences in stromal cell dynamics during CRC metastasis

A. Pathway enrichment analysis with published inflammatory signatures in myCAFs and iCAFs. **B.** UMAP plot of myCAFs and iCAFs identified by joint application of RCA and CCA and color-coded by cell subtype (upper panel). Proportions of cell subtypes in PT, LM and PC tissue (lower panel) on average are shown. **C.** Expression level of an apCAF gene score (Table S4) in CAFs from PT, LM and PC depicted as violin plot. **D.** Expression of the top 3 differentially expressed genes involved antigen presentation in CAFs of PT, LM and PC centred to the average expression of each gene across all locations. The dot size represents the proportion of expressing cells in each cluster. **E.** Differential numbers of L-R interactions between CAFs and tumour cells in LM compared to PC. green: upregulation in PC compared to LM. blue: downregulation in PC compared to LM. **F.** Expression level of significantly upregulated exemplary L or R genes in PC compared to LM. Depicted as stacked violin plot. **G.** Significantly upregulated ligand-receptor pairs between CAFs and tumour cells in PC compared to LM. Depicted as circle plot. **H.** Pathway enrichment analysis in endothelial cells from LM and PC with published gene signatures. **I.** Expression level of significantly upregulated exemplary genes involved in inflammation and proliferation in PC and LM. Depicted as stacked violin plot. **J.** Expression level of an "antigen presentation" and "angiogenesis" gene score (Table S4) in endothelial cells from LM and PC depicted as ridge plot. ****p<0.0001, ***p<0.001, ** p<0.01, * p<0.05, Student's T-test.

A Immune cells - scRNA-seq

15,714 Cd11b- immune cells

Mast cells

NK cells

T cells

B cells

UMAP2

UMAP1

- NK cells
- T cells
- B cells
- Mast cells

PT
LM
PC

0   25   50   75   100
Cell proportions (%)

B T cell subtypes and NK cells - scRNA-seq

UMAP2

UMAP1

- NK cells
- NKT cells
- Trm Cd8 T cells
- Exhausted Cd8 T cells
- Isg Cd8 T cells
- Cytotoxic Cd8 T cells
- Naive Cd8 T cells

- Naive Cd4 T cells
- Th1 Cd4 T cells
- Th2 Cd4 T cells
- Treg Cd4 T cells
- gdT cells

PT
LM
PC

0   25   50   75   100
Cell proportions (%)

C OXPHOS activity

Metabolic Pathway Enirichment

1.0
0.5
0.0

*** ***   *** ***

T cells   NK cells

- PT
- LM
- PC

D Location specific exhaustion and activity of infiltrative CD8 T cells

Genes

Tigit
Tox
Havcr2
Pdcd1
Ctla4
Gzmb
Gzma
Ifng
Prf1

exhaustion

activity

Cytotoxic Cd8 T cells_PT
Cytotoxic Cd8 T cells_LM
Cytotoxic Cd8 T cells_PC

Percent Expressed
- 0
- 20
- 40
- 60
- 80

Average Expression
1.0
0.5
0.0
-0.5
-1.0

(p<0.05)

E NK cells degranulation

Gzmb

Expression Level
4
3
2
1
0

*** ***

Prf1

Expression Level
3
2
1
0

*** ***

- PT
- LM
- PC

Figure 4: Location-specific anti-tumoural immunity during CRC metastasis

A. UMAP plot of 15,714 $CD45^+$ / $CD11b^-$ immune cells identified by joint application of RCA and CCA and color-coded by cell subtype (upper panel). Proportions of all cell types in PT, LM and PC (lower panel) on average are shown. **B.** UMAP plot of T and NK cells identified by joint application of RCA and CCA and color-coded by cell type (upper panel). Proportions of all cell types in PT, LM and PC (lower panel) on average are shown. **C.** Metabolic activity analysis in T cells and NK cells of PT, LM and PC. Metabolic score depicted as boxplot. **D.** Expression of significantly differentiated genes involved in activity and exhaustion of cytotoxic $CD8^+$ T cells from PT, LM and PC, centred to the average expression of each gene across all locations. The dot size represents the proportion of expressing cells in each cluster. $p<0.05$. **E.** Expression level of Gzmb and Prf1 in NK cells from PT, LM and PC depicted as violin plot. ***$p<0.001$, Student's T-test.

A B cell subtypes - scRNA-seq

- Irf4+ B cells
- Ccr7+ B cells
- Immature B cells
- Memory B cells
- IgM Plasma cells
- IgG Plasma cells
- Cd38+ IgG Plasma cells
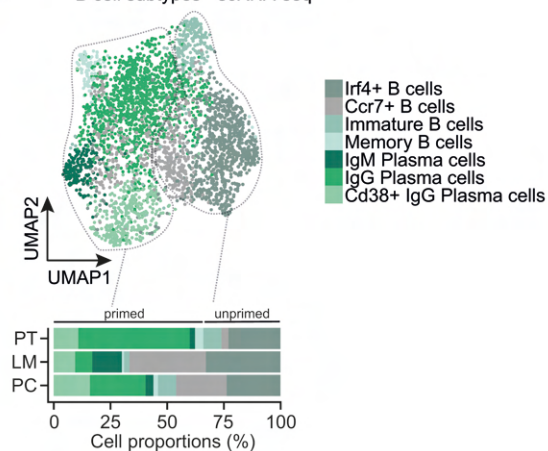
B Reduction of outgoing B cell signaling in MET compared to PT

Count
- 200
- 300
- 400
- 500
- 600

- Irf4+ B cells
- IgM Plasma cells
- IgG Plasma cells
- Cd38+ IgG Plasma cells
- Ccr7+ B cells
- Memory B cells
- Immature B cells

C Summarized communication pathways

coloured text: p<0.05

- PT
- MET
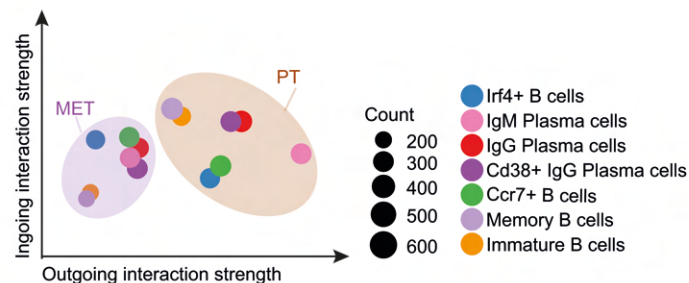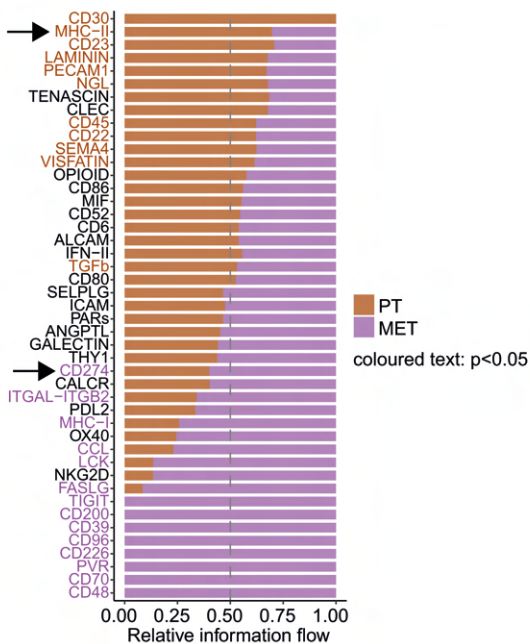
D B cell dependent MHC-II signaling network in PT and MET
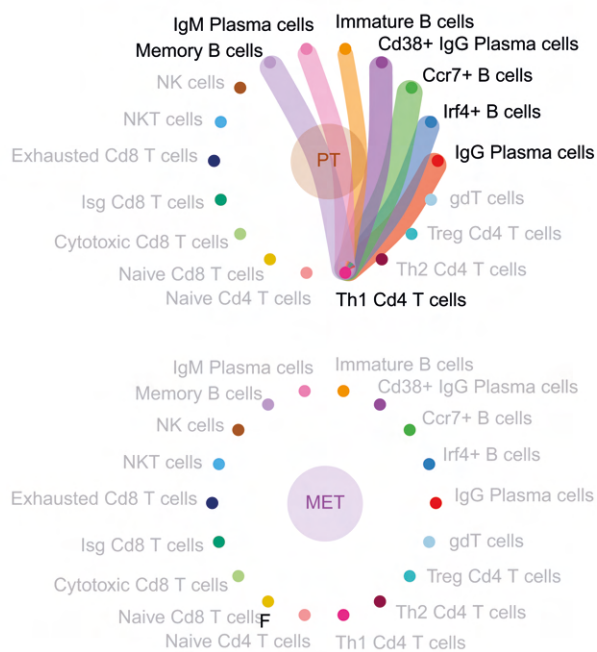
Figure 5: Impairment of B cell networks in metastasized CRC

A. UMAP plot of 3,355 B cells identified by joint application of RCA and CCA and color-coded by cell subtype (upper panel). Proportions of all cell sub types in PT, LM and PC (lower panel) on average are shown. Dashed lines mark primed and unprimed / immature B cell subtypes. **B.** Ingoing and outgoing interaction strength of B cells with joint projection and clustering B cell subtypes onto shared two-dimensional manifold according to their local descent. MET: Combined analysis for LM and PC. Circle or square size is proportional to the signalling strength of respective cellular subtype. Different colours represent different B cell subtypes. **C.** Unbiased overall information flow of signalling networks by summarizing all the communication probabilities in respective network. All the significant signalling pathways were ranked based on their differences of overall information flow within the inferred networks between PT and MET. Brown: enriched in PT. Purple: enriched in MET. **D.** Significant ligand-receptor pairs of the MHC-II signalling network between B cell subtypes and Th1 Cd4$^+$ T cells in PT and MET. The edge width represents MHC-II dependent communication probability.

A — Increased Th2 dependent metastatic PD-L1 signaling
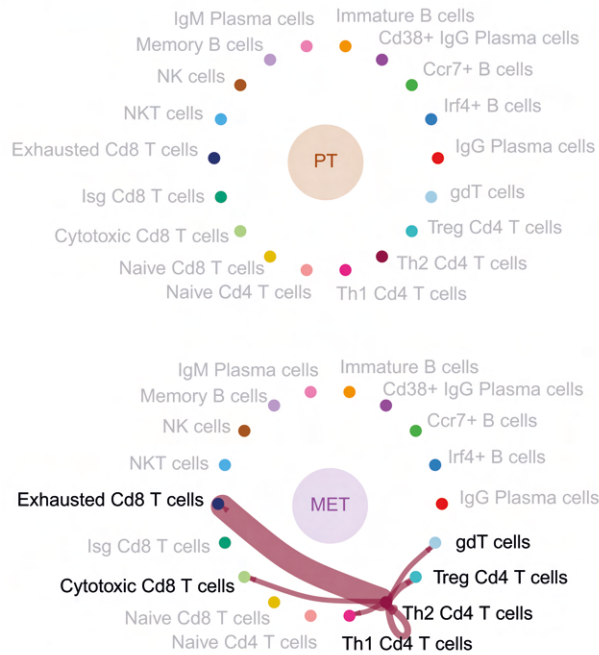
B — Differential number of interactions in LM and PC
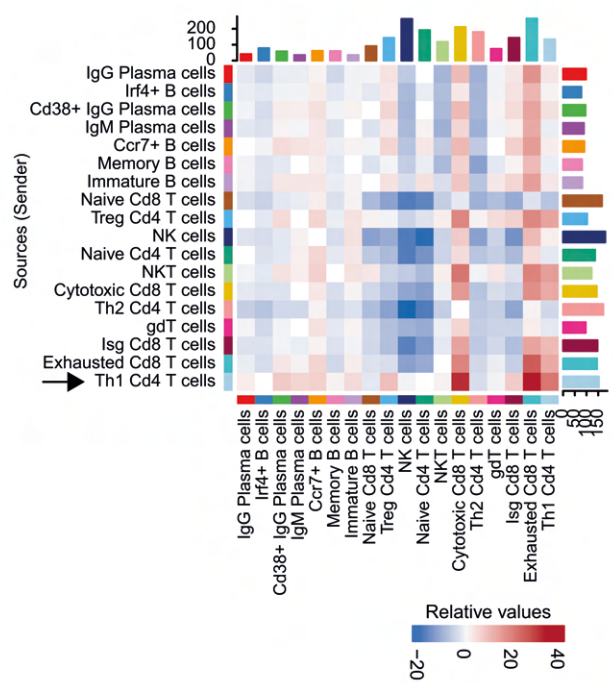
C — Differential signaling capacity of Th1 Cd4 T cells in PC
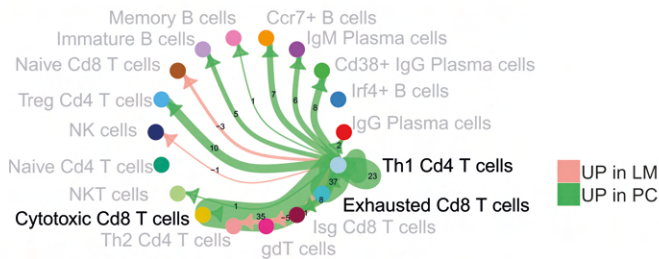
D — Th1 Cd4 T cells checkpoint inhibition
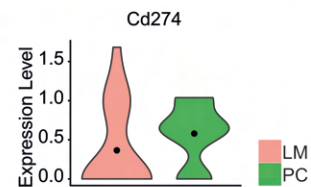
Figure 6: Inter-metastatic alterations of adaptive immune responses multivisceral CRC

A. Significant ligand-receptor pairs of the PD-L1 signalling network between Th2 Cd4$^+$ T cells and other T cell subtypes in PT and MET. The edge width represents MHC-II dependent communication probability. **B.** Heatmap depicting the differential number of interactions between B and T cell subtypes in LM and PC. Colours represent relative values. **C.** Differential numbers of L-R interactions between Th1 Cd4$^+$ T cells and B cell and T cell subtypes in LM compared to PC. Green: upregulation in PC compared to LM. Red: upregulation in LM compared to PC. Numbers indicate differentially regulated L-R pairs. **D.** Expression level of *Cd274* in PC compared to LM. Depicted as violin plot.

A Experimental overview
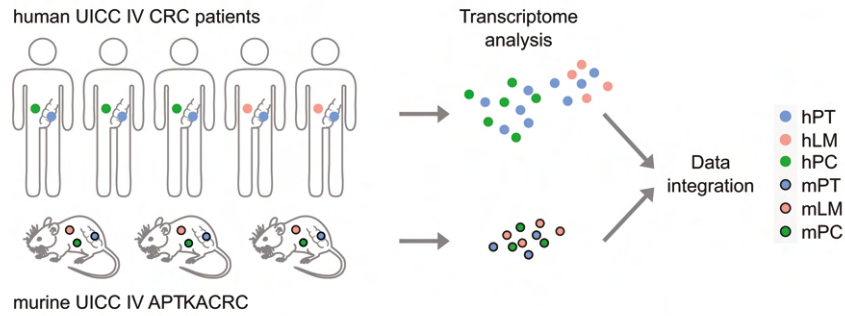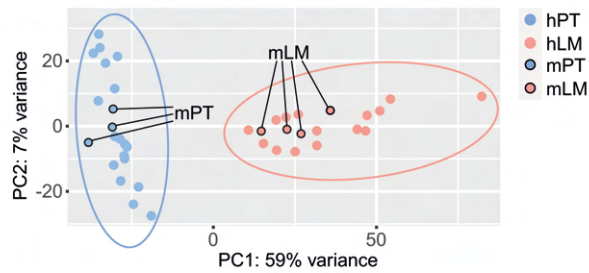
human UICC IV CRC patients

Transcriptome analysis

Data integration

- hPT
- hLM
- hPC
- mPT
- mLM
- mPC

murine UICC IV APTKACRC

B Location dependent clustering of PT and LM

PC2: 7% variance

PC1: 59% variance

mLM

mPT

- hPT
- hLM
- mPT
- mLM

C Immunological deconvolution of murine and human LM

Tumoural MCP score

- APTKA LM
- human LM

T cell, cytotoxicity score, NK cell, B cell, macrophages, Myeloid dendritic cell

n.s., n.s., n.s., *, n.s., *

D Location dependent clustering of PT and PC

PC2: 9% variance

PC1: 14% variance

mPC

mPT

- hPC
- hPT
- mPC
- mPT

E Immunological deconvolution of murine and human PC

Tumoural MCP score

- APTKA PC
- human PC

macrophages, dendritic cells, B cells, NK cells activated, T cells, cytotoxicity score

*, n.s., *, ***, n.s., n.s., n.s., n.s., *
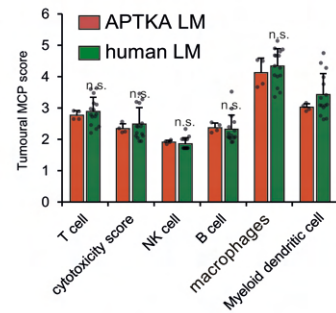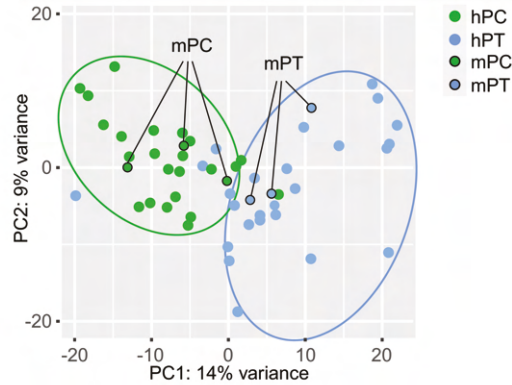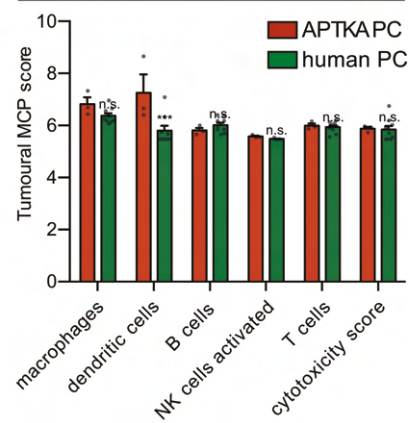
Figure 7: Murine multivisceral APTKA CRC mimics human stage IV CRC

A. Experimental overview for integrated comparison of human and murine RNA-Seq data from PT and PC. **B.** Batch-corrected principal component analysis (PCA) of 15 patient-matched hPT/hLM samples and three mPT / four mLM samples show location dependent clustering of human and murine transcriptomes. **C.** Estimated MCP scores reflecting immune cell infiltration in RNA samples from murine and human LM. **D.** Batch-corrected principal component analysis (PCA) of 25 patient-matched hPT/hPC samples and three mPT/mPC samples show location dependent clustering of human and murine transcriptomes. **E.** Estimated MCP scores reflecting immune cell infiltration in RNA samples from murine and human PC. ***p<0.001, n.s. not significant, Student's T-test.

A mouse PC - GSEA

Enrichment plot:
HALLMARK_EPITHELIAL_MESENCHYMAL_TRANSITION

NES: 2.19
FDR: 0.0

B human PC - GSEA

Enrichment plot:
HALLMARK_EPITHELIAL_MESENCHYMAL_TRANSITION

NES: 2.65
FDR: 0.0

C Mesenchymal phenotype of murine PC

D Mesenchymal phenotype of human PC

E Spatial origin of mesenchymal marker expression in murine and human CRC - IHC
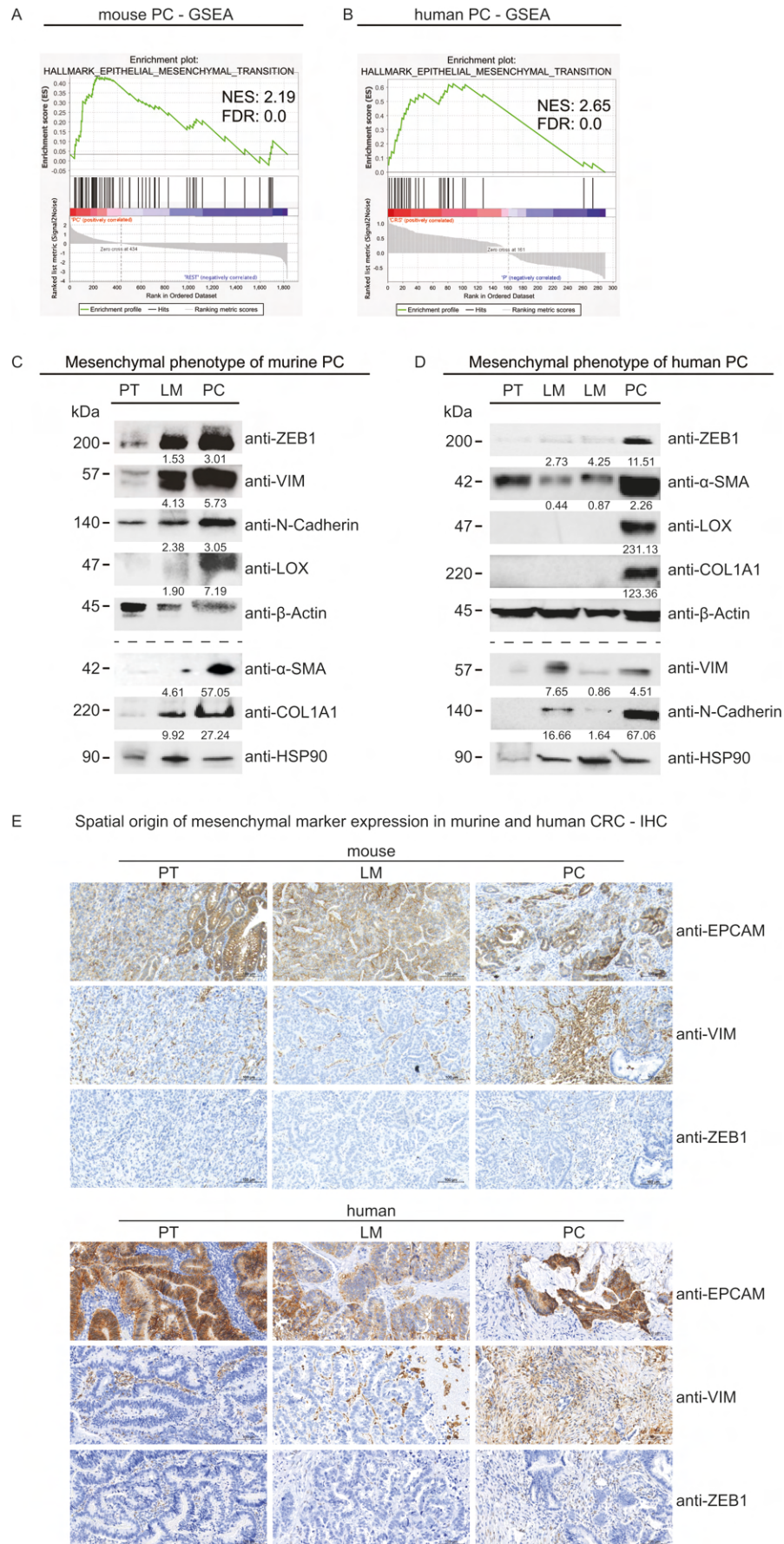
Figure 8: PC is associated with a mesenchymal phenotype in human and murine CRC

A, B. GSEA (Signal2Noize) with Hallmark EMT gene signature in murine and human PC. NES: normalized expression score. FDR: false discovery rate. **C.** Representative Western blot showing expression of depicted proteins in lysates from murine PT, LM and PC. Fold change normalised to respective loading control (upper panel: β-Actin, lower panel: HSP-90) and PT. The experiment was performed twice. **D.** Western blot showing expression of depicted proteins in representative lysates from human PT, LM and PC. Fold change normalised to respective loading control (upper panel: β-Actin, lower panel: HSP-90) and PT. The experiment was performed twice. **E.** Representative IHC of murine and human PT, LM and PC for EPCAM, VIM and ZEB1. IHC was performed on 10 tissue samples of each location.

A Experimental overview: intraperitoneal anti-PD1 therapy

B TME reconstitution by intraperitoneal anti-PD1 therapy in PC

C Cell death induction of tumour cells in PC tissue by intraperitoneal anti-PD1 therapy
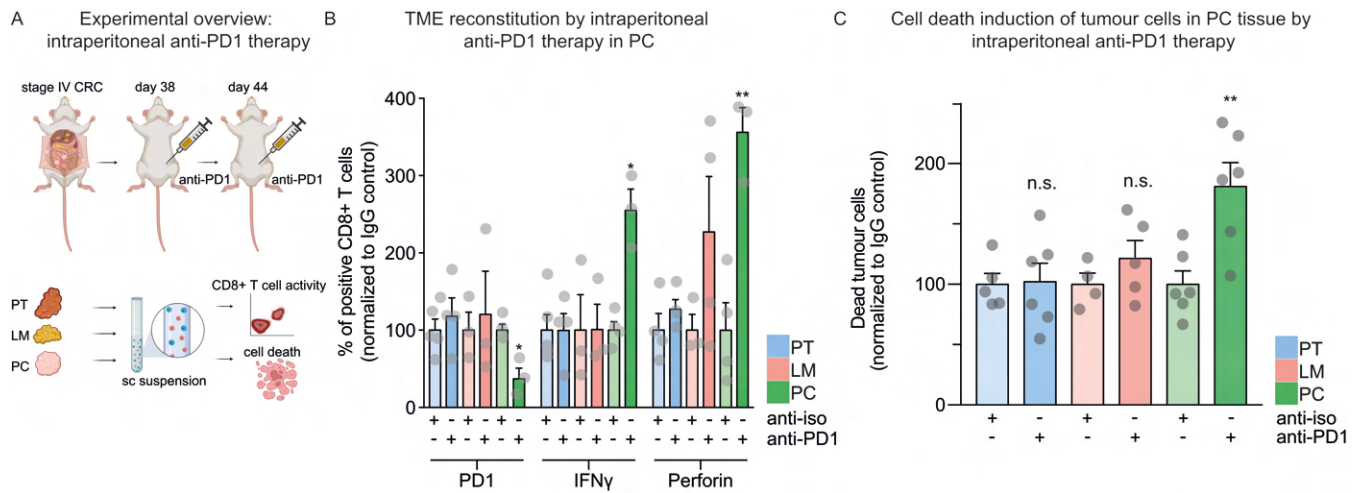
D B cell and T effector cell reconstitution by intraperitoneal anti-PD1 therapy in PC - representative IHC
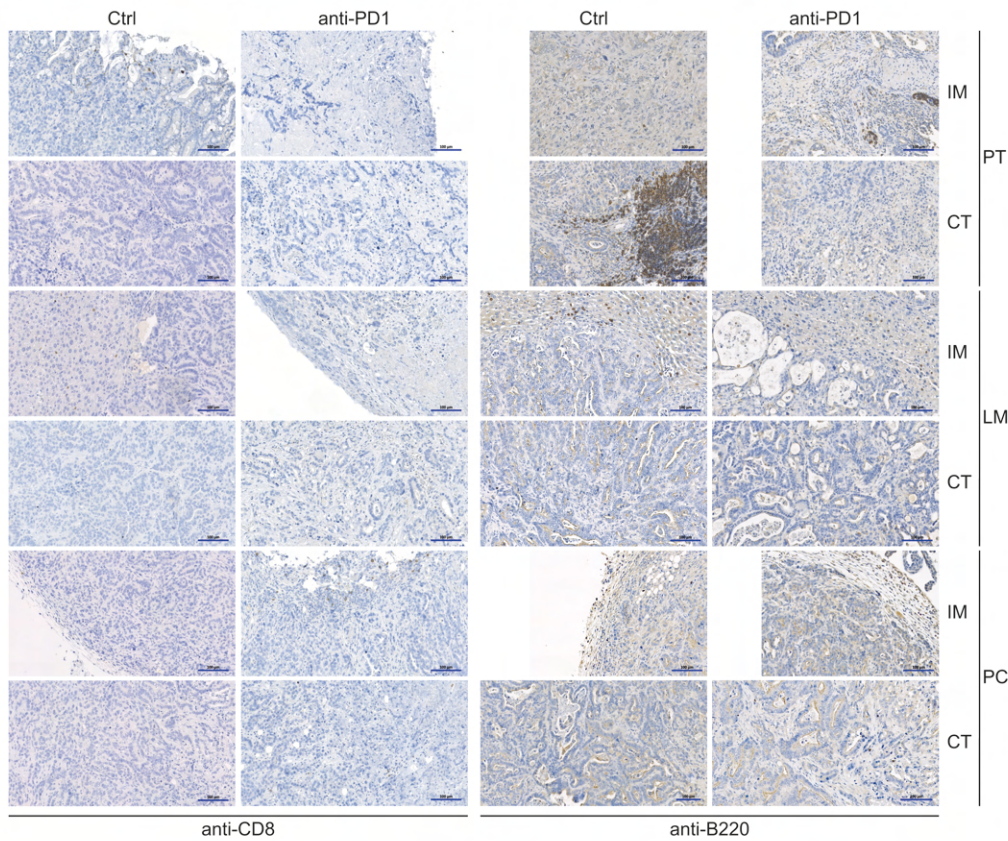
E Location dependent quantification of T effector cells
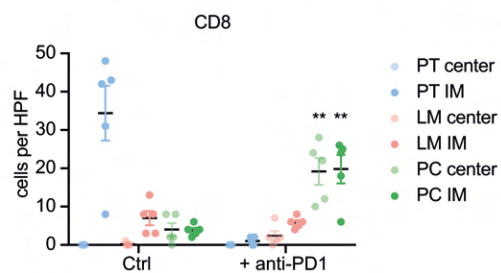
F Location dependent quantification of B cells
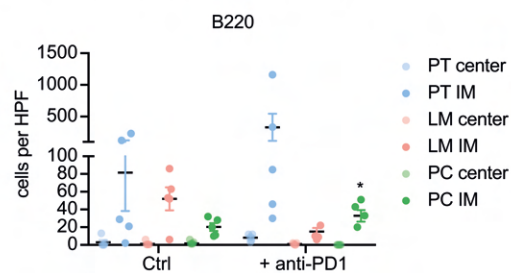
Figure 9: Intraperitoneal application of ICB reconstitutes effector T cell function in PC and emphasizes the importance of a site-specific CRC therapy

A. Experimental overview of stage IV CRC treatment by intraperitoneal application of anti-PD1 therapy. **B.** Quantification of changes in CD8$^+$ T cell regulation upon ICB by FACS. Normalized to IgG control, in %. n=3-5 per group. **C.** Quantification of changes in epithelial cell death (EPCAM$^+$/Zombie$^+$ cells) upon ICB by FACS. Normalized to IgG control, in %. n=4-6 per group. **D.** Representative IHC of murine PT, LM and PC at the invasive margin (IM) and tumour center (CT) for CD8 and b220 with and without anti-PD1 treatment. IHC was performed on 5 tissue samples for each location and antibody.

E. Quantification of CD8$^+$ cells with and without ICB in PT, LM and PC tissue at both IM and CT (n=3-5). **F.** Quantification of b220$^+$ cells with and without ICB in PT, LM and PC tissue at both IM and CT (n=3-5). ** $p<0.01$, * $p<0.05$, Student's T-test.

A Experimental overview

APTAK organoids in collagen dome

surgical transplantation of tumor organoids under the serosa of the cecum

cecum

tumor growth

organoids in collagen dome

liver metastasis
peritoneal carcinomatosis
primary tumor
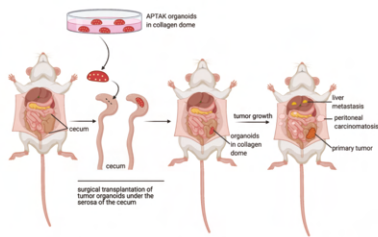
B APTKA organoid preparation
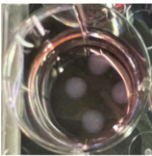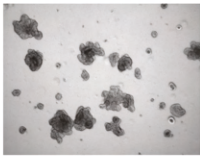
Matrigel domes | APTKA organoids in vitro | APTKA single cells in collagen
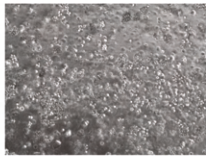
C Subserosal surgical transplantion of APTKA organoids into the murine cecum wall

1 2 3 4 5 6
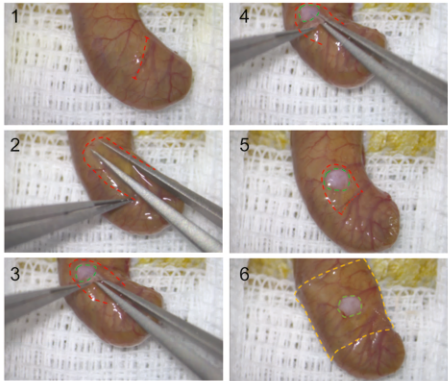
D Modified PCI scoring system

I II
III IV
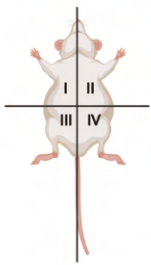
score of each quadrant = 0
+ (no. small tumor x 1)
+ (no. middle tumor x 2)
+ (no. large tumor x 3)

Score I = _____
Score II = _____
Score III = _____
Score IV = _____

PCI (sum of I – IV) = [ ]

E Peritoneal tumour load upon orthotopic APTKA transplantation

Peritoneal tumour load (mod. PCI)

APTKA transplantation
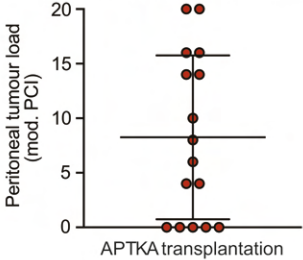
F Consensus molecular subtype gene expression profiling

	prediction	FDR
PT1	CMS4	0.003
PT2	NA	0.057
PT3	CMS4	0.003

G iCMS of location dependent tumour epithelium

**** ****

iCMS2 score up

****

iCMS3 score up

PT
LM
PC
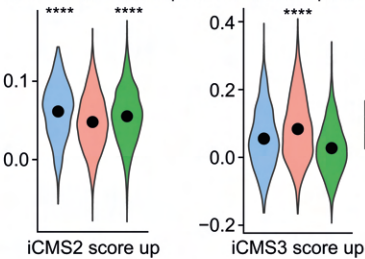
H Absolute cellcounts in PT, LM and PC tissue

Absolute cellcounts

PT LM PC

Tumour cells
B cells
T cells
Myeloid cells
CAFs
Endothelial cells
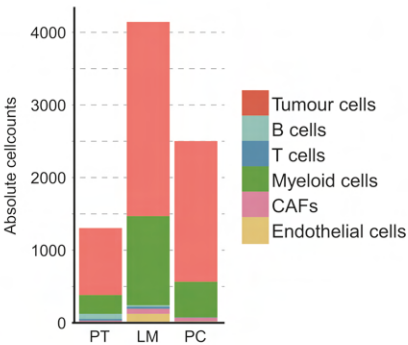
I Representative IHC of multivisceral murine APTKA CRC
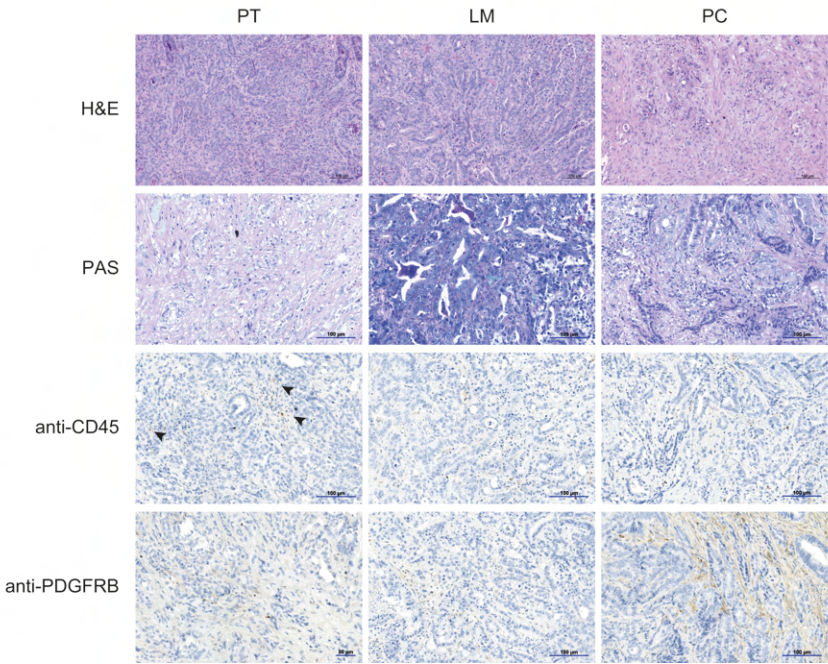
PT LM PC

H&E

PAS

anti-CD45

anti-PDGFRB

Supplementary Figure 1: A distinct cellular and functional landscape of murine primary CRC, liver metastases and peritoneal carcinomatosis

A. Experimental overview for orthotopic subserosal APTKA transplantation. **B.** Representative images of APTKA organoids in matrigel domes during cultivation in vitro (left panel). Day six after passaging (middle panel). Single cells from APTKA organoids embedded in 10µl collagen dome before one day before surgical subserosal cecum transplantation into mice (right panel). **C.** Representative images of the surgical subserosal transplantation of APTKA tumour organoids into the cecum. 1. The cecum is exteriorized and embedded on a wet pad. The red dashes line marks the incision line of the cecum serosa. 2 After incision, the serosa is lifted and a deep subserosal pocket which can fully cover the 10µl collagen dome containing the APTKA organoid cells is formed (red dashed line). 3. Placement of the collagen dome (green dashed line) into the preformed subserosal pocket. 4. Deep implantation of the collagen dome for complete coverage by the cecum serosa. 5. Deeply implanted and fully covered collagen dome in the subserosal pocket. 6. Pre-cut rectangle of an adhesion barrier (yellow dashed line) is placed over the transplantation site and the cecum is wrapped with the film to secure the collagen dome and to prevent adhesions during wound healing. For detailed surgical steps, also see Movie S1. **D.** Schematic representation of the modified peritoneal carcinomatosis index (PCI). **E.** Laparoscopically analysed PCI eight weeks after orthotopic APTKA transplantation. **F.** Consensus molecular subtype of PT according to bulk transcriptome-based analyses. **G.** Violin plot depicting expression of scores for marker genes of iCMS2 and iCMS3. ****p<0.0001, Student's T-test. **H.** Absolute numbers for respective celltypes in PT, LM and PC. **I.** H&E staining, periodic acid–Schiff reaction

(PAS) and IHC of murine PT, LM and PC for CD45 (immune cells) and PDGFRB (stromal

cells). Histology and IHC was performed on 10 slides for each location.

A   Intraepithelial communication patterns in PT, LM and PC of CRC
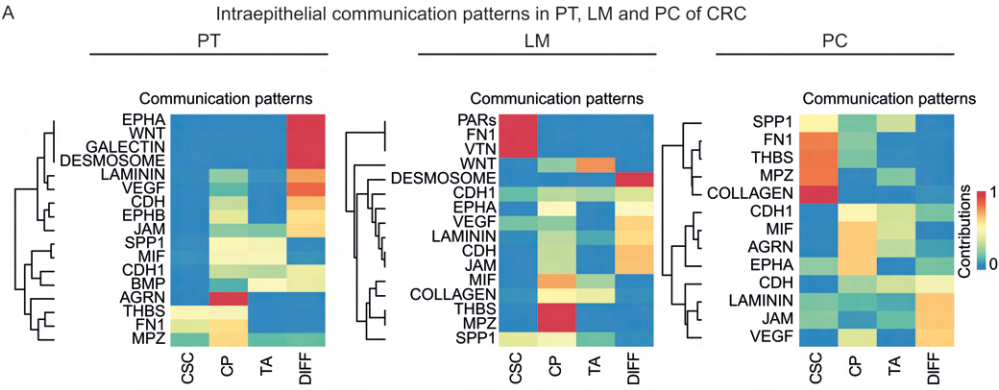
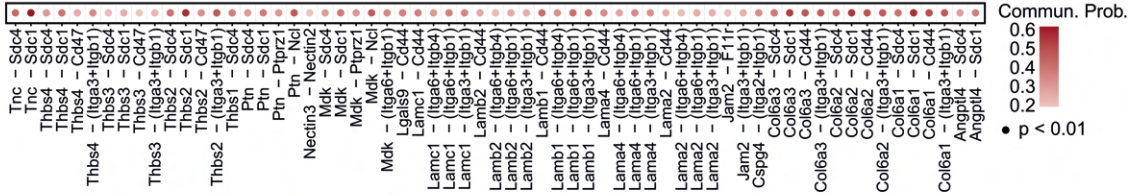**B**   CSC dependent L-R pairs in PT, LM and PC
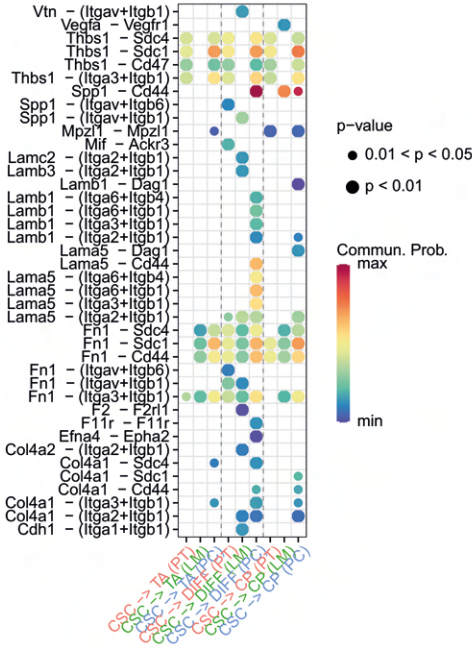
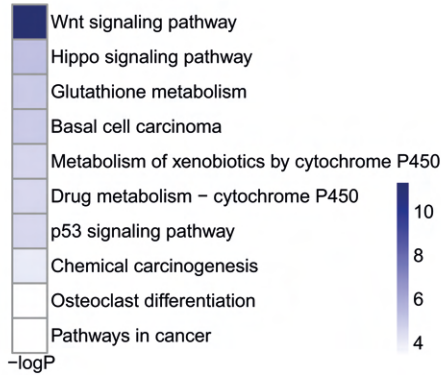**Supplementary Figure 2: Location-specific metabolic reprogramming of the STEM compartment in multivisceral CRC**

A. Intraeptihelial communication patterns between cellular subtypes. Heatmap shows the correspondence between the inferred patterns and cell subtypes, as well as signalling pathways. **B.** Location dependent comparison of the significant ligand-receptor pairs between CSC, CP, TA and DIFF. The dot color reflects communication probabilities and dot size represents computed p-values. Empty space means the communication probability is zero.

A   CAF subclustering

C1
C2

PT
LM
PC
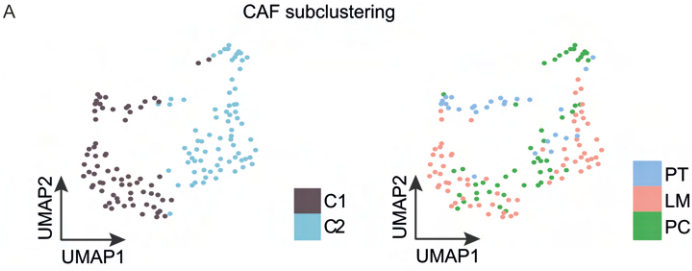
B   Increased communication probability between CAFs and epithelial CRC cells in PC compared to LM tissue

Commun. Prob.
0.6
0.5
0.4
0.3
0.2

● p < 0.01

C   Enhanced pathway activity in PC CSCs
-GO Kegg-

Wnt signaling pathway
Hippo signaling pathway
Glutathione metabolism
Basal cell carcinoma
Metabolism of xenobiotics by cytochrome P450
Drug metabolism − cytochrome P450
p53 signaling pathway
Chemical carcinogenesis
Osteoclast differentiation
Pathways in cancer

−logP

10
8
6
4

Supplementary Figure 3: Inter-metastatic differences in stromal cell dynamics during CRC metastasis

A. UMAP plot of CAFs subclusters identified by joint application of RCA and CCA and color-coded by cluster (left panel). UMAP plot of CAFs color-coded by location (right panel). **B.** Significantly increased communication probabilities for L-R pairs between CAFs and tumour cells in LM and PC. The colour represents the communication probability, dot size represents significancy levels. **C.** Unbiased KEGG pathway enrichment analysis with differentially regulated genes (p adj. <0.05) in PC CSCs compared to LM CSCs.

A Myeloid compartment - scRNA-seq

cDC
Mki67+ Macrophages
Mrc1+ Macrophages
Spp1+ Macrophages
non classical Monocytes
Hsp+ Monocytes
Neutrophiles
Inflamed tissue Macrophages
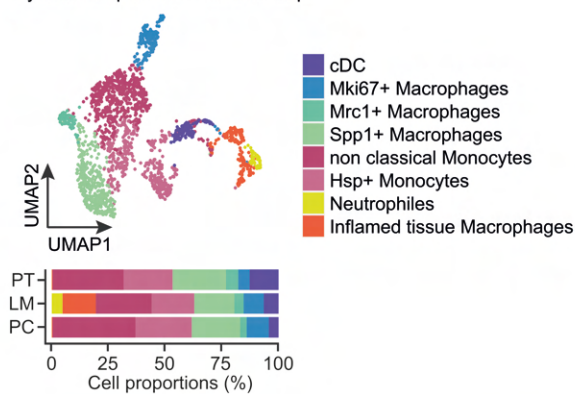
B Metastatic Mrc1+ macrophages - immuno suppressive phenotype
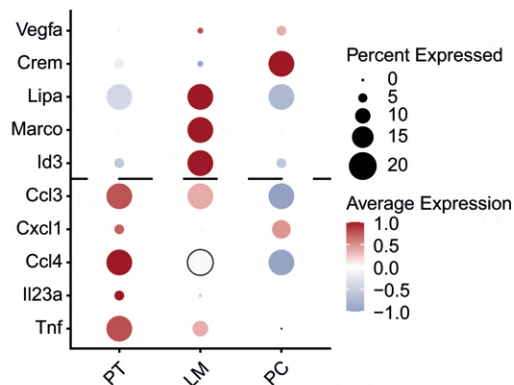
C Gating strategy - FACS sorting
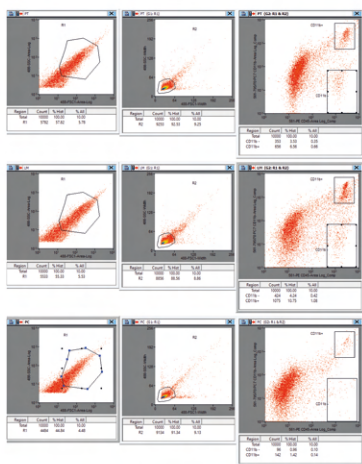
D Mitochondrial gene expression after QC
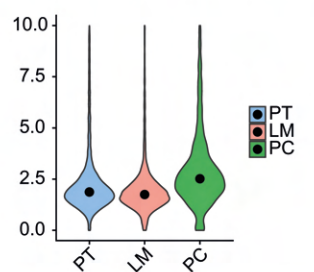
E nFeature after QC
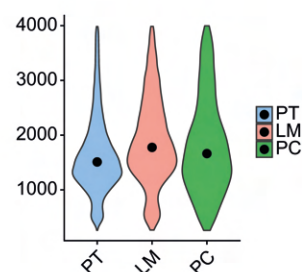
F T cell subtypes and NK cells - marker gene expression
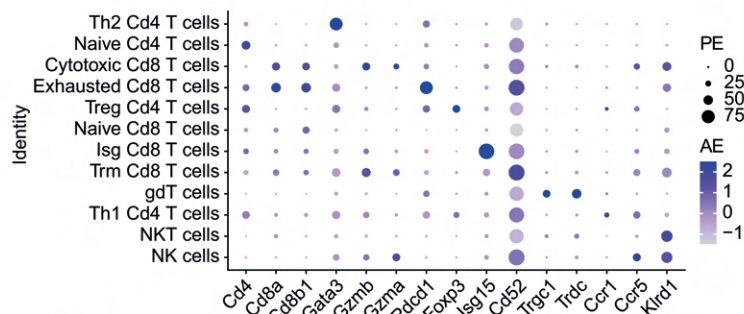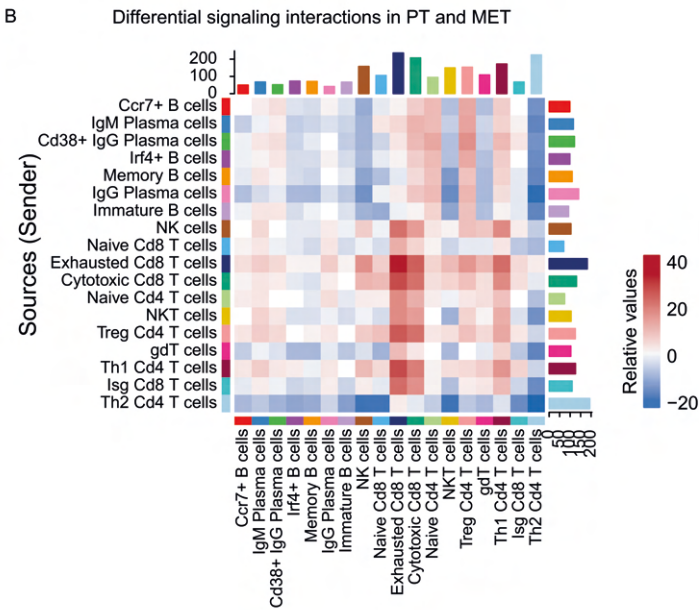
G Immune cell subtypes - scRNA-seq
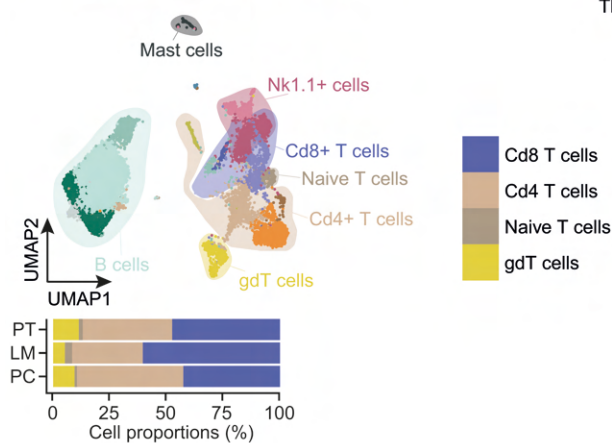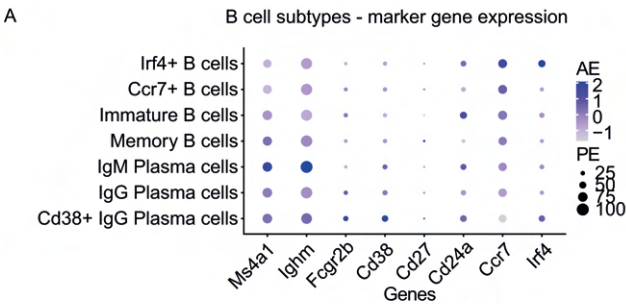
H OXPHOS activity
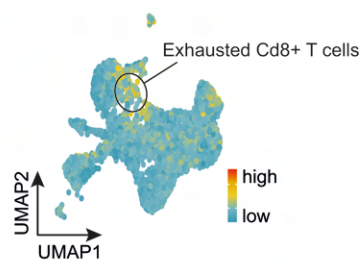
I Site specific OXPHOS activity in infiltrative T cell subtypes
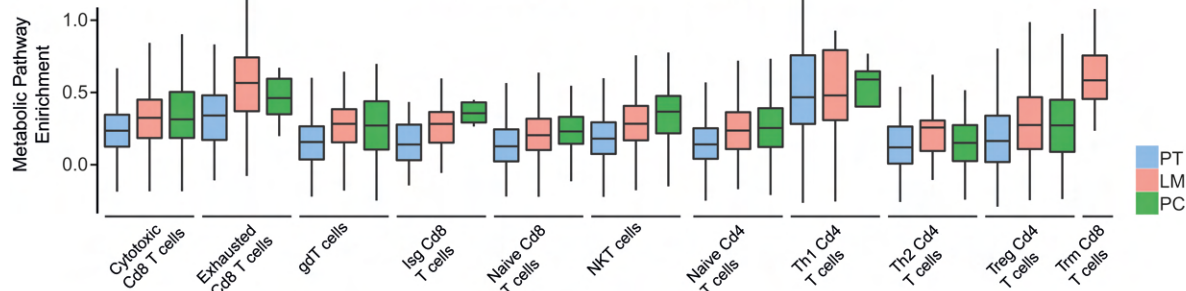
**Supplementary Figure 4: Location-specific anti-tumoural immunity during CRC metastasis**

A. UMAP plot of myeloid cell subtypes identified by joint application of RCA and CCA and color-coded by cell type (upper panel). Proportions of myeloid cell subtypes in PT, LM and PC (lower panel) on average are shown. **B.** Expression of genes involved in polarization of $Mrc1^+$ macrophages from PT, LM and PC, centred to the average expression of each gene across all locations. The dot size represents the proportion of expressing cells in each cluster. **C.** Gating strategy for FACS guides isolation of $CD45^+$ / $CD11b^-$ immune cells from whole tumour single cell suspensions from PT (upper panel), LM (middle panel) and PC (lower panel). **D.** Mitochondrial gene expression after QC for each sample depicted as violin plot. **E.** nFeature after QC for each sample depicted as violin plot. **F.** Canonical marker gene expression for multiple T cell subtypes and NK cells centred to the average expression of each gene across cells. The dot size represents the proportion of expressing cells in each cluster. PE: percent expressed. AE: average expression. **G.** UMAP plot of B cells, mast cells, T cells and NK cells identified by joint application of RCA and CCA and color-coded by cell type (upper panel). Proportions of T cell subtypes in PT, LM and PC tissue (lower panel) on average are shown. **H.** UMAP of metabolic scores for OXPHOS in T cell subtypes. **I.** Metabolic activity analysis in the T cell compartment of PT, LM and PC on cell subtype level. Metabolic score depicted as boxplot.

A B cell subtypes - marker gene expression

B Differential signaling interactions in PT and MET

C Celltype and location dependent PD-L1 and PD1 expression
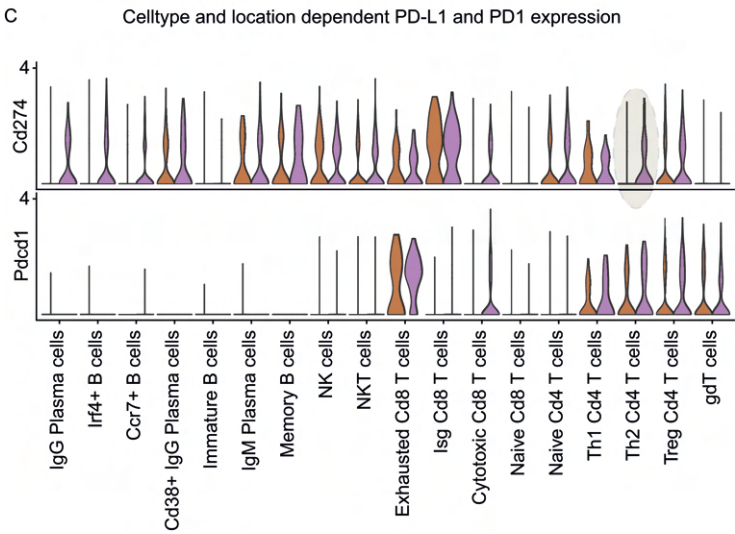
Supplementary Figure 5: Impairment of B cell networks in metastasized CRC

A. Canonical marker gene expression for multiple B cell subtypes centred to the average expression of each gene across all cells. The dot size represents the proportion of expressing cells in each cluster. PE: percent expressed. AE: average expression. **B.** Heatmap depicting the differential number of interactions between B cell and T cell subtypes in PT and MET. Colours represent relative values. **C.** Expression level of *Cd274* and *Pdcd1* in B cell and T cell subtypes from PT and MET depicted as violin plot.

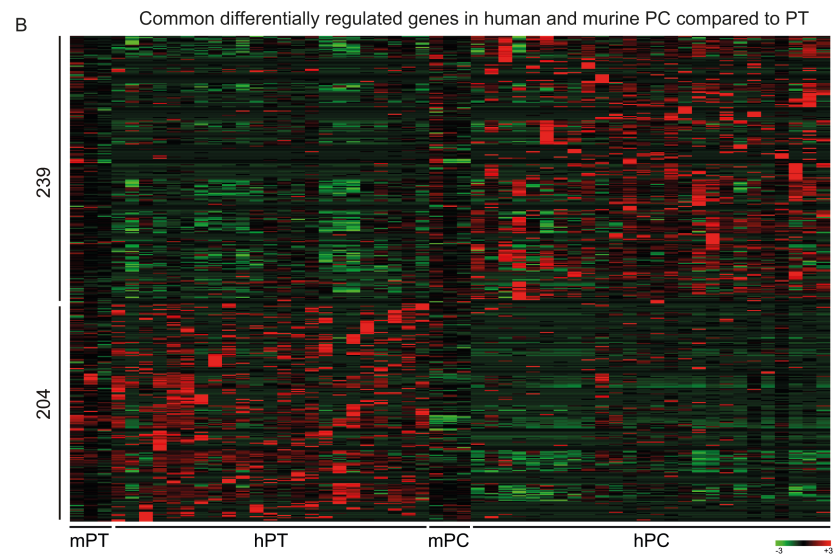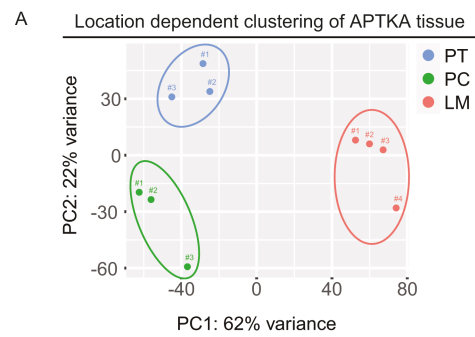A   Differential Th1 dependent PD-L1 signaling in LM and PC
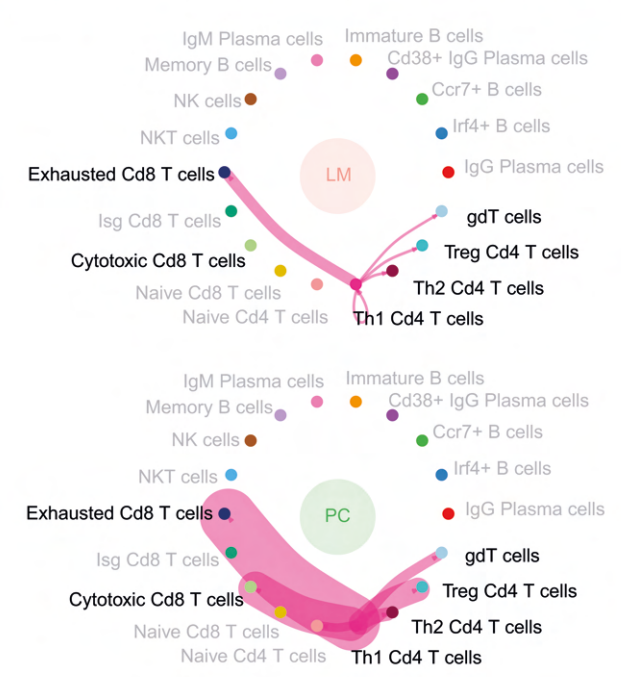
B   Summarized communication pathways
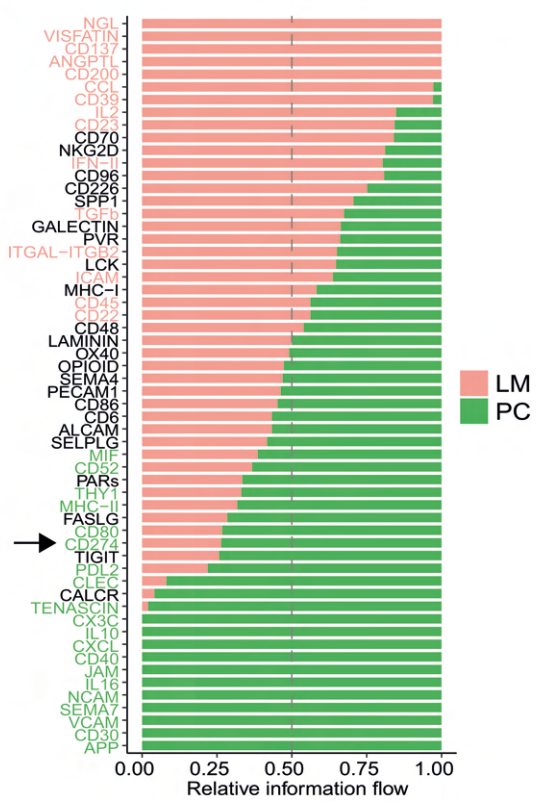
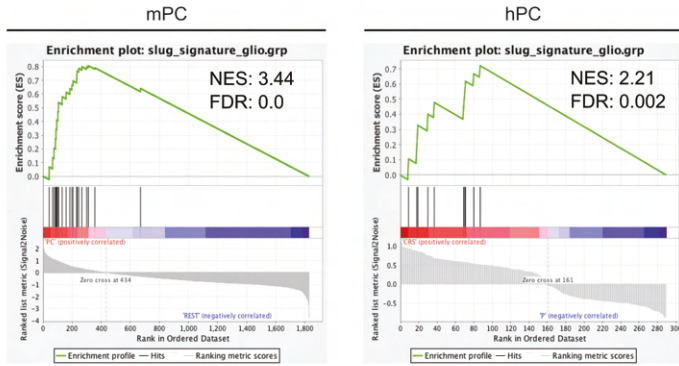**Supplementary Figure 6: Inter-metastatic alterations of adaptive immune responses multivisceral CRC**

A. Unbiased overall information flow of signalling networks by summarizing all the communication probabilities in respective network. All the significant signalling pathways were ranked based on their differences of overall information flow within the inferred networks between LM and PC. Signalling pathways coloured by red are more enriched in LM, pathways coloured by green were enriched in PC. **B.** Significant ligand-receptor pairs of the PD-L1 signalling network between Th1 CD4$^+$ T cells and other T cell subtypes in LM and PC. The edge width represents MHC-II dependent communication probability.
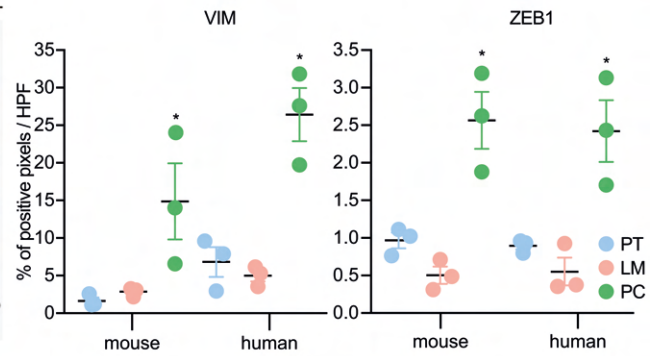
A

Location dependent clustering of APTKA tissue

PC1: 62% variance

PC2: 22% variance

PT
PC
LM

B

Common differentially regulated genes in human and murine PC compared to PT

239

204

mPT   hPT   mPC   hPC

-3 +3

Supplementary Figure 7: Murine multivisceral APTKA CRC mimics human stage IV CRC

A. Principal component analysis (PCA) of three PT, three LM and four PC tissues show location dependent clustering of transcriptomes. **B.** Heatmap depicting common differentially regulated genes in human and murine PC compared to PT. p adj. <0.05.

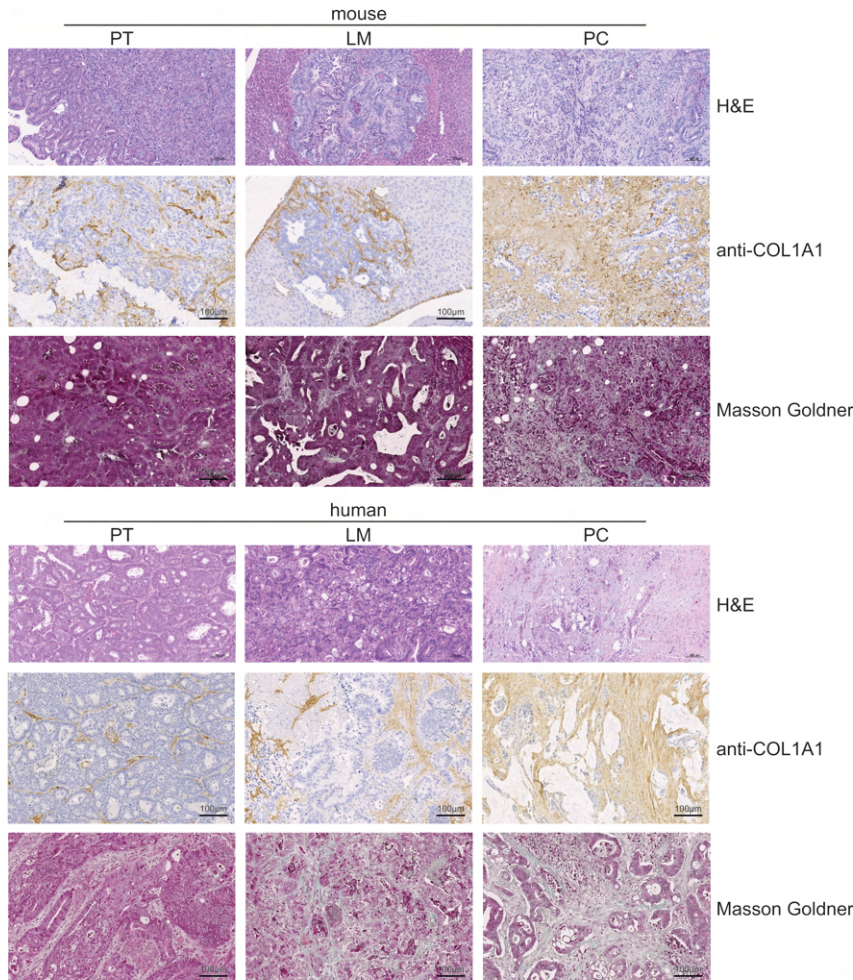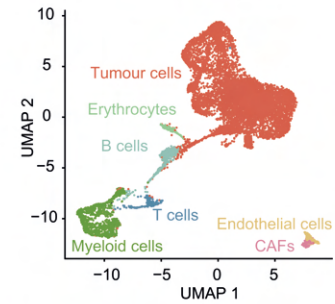A — Location dependent gene set enrichment

mPC — Enrichment plot: slug_signature_glio.grp — NES: 3.44, FDR: 0.0

hPC — Enrichment plot: slug_signature_glio.grp — NES: 2.21, FDR: 0.002

B — Mesenchymal marker gene expression from IHC - quantification

VIM

ZEB1

PT / LM / PC

C — Fibrosis in murine and human CRC - IHC
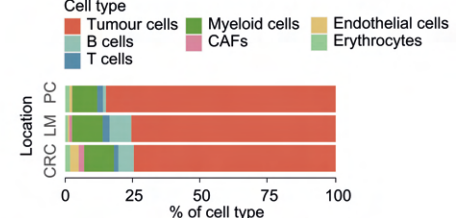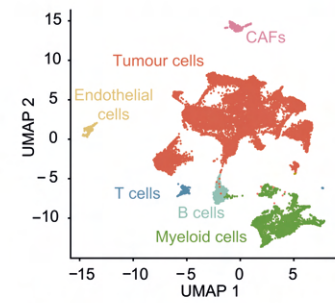
mouse — PT / LM / PC — H&E / anti-COL1A1 / Masson Goldner

human — PT / LM / PC — H&E / anti-COL1A1 / Masson Goldner

D — human scRNA-Seq

Tumour cells, Erythrocytes, B cells, T cells, Endothelial cells, CAFs, Myeloid cells

E — human scRNA-Seq

Cell type: Tumour cells, B cells, T cells, Myeloid cells, CAFs, Endothelial cells, Erythrocytes

F — human+mouse scRNA-Seq

CAFs, Tumour cells, Endothelial cells, T cells, B cells, Myeloid cells

G — human+mouse scRNA-Seq

Cell type: Tumour cells, B cells, T cells, Myeloid cells, CAFs, Endothelial cells, Erythrocytes
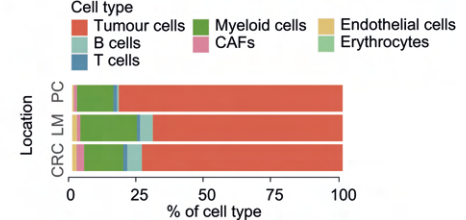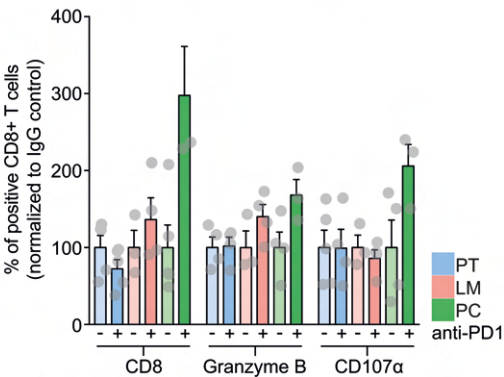
Supplementary Figure 8: Peritoneal carcinomatosis is associated with a mesenchymal phenotype in human and murine CRC

A. GSEA (Signal2Noize) with published Slug gene signature in murine and human PC. NES: normalized expression score. FDR: false discovery rate. **B.** Quantification of VIM and ZEB1 in IHC stainings of murine PT, LM and PC samples per HPF (n=3). * p<0.05, Student's T-test. **C.** Representative IHC of murine and human PT, LM and PC for COL1A, as well as Masson Goldner staining. **D.** UMAP plot of human CRC tissue identified by joint application of RCA and CCA and color-coded by cell type. **E.** Proportions of all cell types in human PT, LM and PC on average are shown. **F.** UMAP plot of integrated human and murine CRC identified by joint application of RCA and CCA and color-coded by cell type. **G.** Proportions of all cell types in integrated human and murine PT, LM and PC on average are shown.
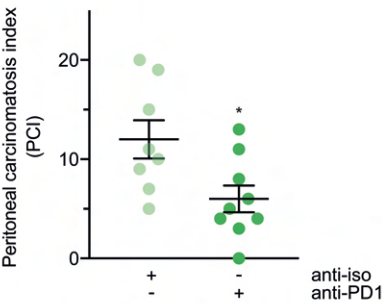
A — TME reconstitution by intraperitoneal anti-PD1 therapy in PC

B — Reduction of intraperitoneal tumour mass by intraperitoneal anti-PD1 therapy

Supplementary Figure 9: Intraperitoneal application of ICB reconstitutes effector T cell function in PC and emphasizes the importance of site-specific CRC therapy

A. Quantification of changes in CD8$^+$ T cell regulation upon intraperitoneal anti-PD1 treatment by FACS. Normalized to IgG control, in %. n=3-5 per group. **B.** Quantification of macroscopic intraperitoneal tumour load (PCI) by diagnostic laparoscopy upon intraperitoneal anti-PD1 treatment (n=8 anti-iso, n=9 anti-PD1). * $p < 0.05$, Student's T-test.

Table S1. Western Blot Antibody list.

target	dilution	blocking	company	catalog number
ACTA2	1:1000	5 % BSA	Cell Signaling Technology	#19245S
ACC1	1:1000	5 % BSA	Cell Signaling Technology	#3676
ACTB	1:1000	5 % skim milk powder	Cell Signaling Technology	#4970S
COL1A1	1:1000	5 % BSA	Cell Signaling Technology	#81375S
CDHE	1:1000	5 % BSA	Cell Signaling Technology	#14472S
FAS	1:1000	5 % BSA	Cell Signaling Technology	#3180
LDHA	1:1000	5 % BSA	Cell Signaling Technology	#3582
LOX	1:1000	5 % skim milk powder	Cell Signaling Technology	#58135S
CDHN	1:1000	5 % BSA	Cell Signaling Technology	#13116S
PDHA1	1:1000	5 % BSA	Cell Signaling Technology	#3205
VIM	1:1000	5 % BSA	Cell Signaling Technology	#5741S

| ZEB1 | 1:1000 | 5 % BSA | Cell Signaling Technology | #70512S |

Table S2. IHC Antibody list.

target	dilution	antigen retrieval	company	catalog number
ACTA2	1:320	citrate	Cell Signaling	#19245S
b220	1:100	citrate	eBioscience	#14-0452-82
CD45	1:100	citrate	Cell Signaling	# 70257S
COL1A1	1:100	citrate	Cell Signaling	#81375S
LOX	1:1000	citrate	Genetex	#GTX03201
PAS Kit	-	-	Abcam	#AB150680
PDGFRB	1:150	citrate	Cell Signaling	#3169S
VIM	1:100	citrate	Cell Signaling	#5741S
ZEB1	1:100	citrate	Cell Signaling	#70512S

Table S3. Flow cytometry Antibody list.

target	fluorochrome	company	catalog number
CD45	Alexa Fluor 700	Biolegend	103128
CD3	Brilliant Violet 421	Biolegend	100227
CD3	Brilliant Violet 785	Biolegend	100231
CD3	biotin	Biolegend	100304
CD4	PerCP Cy5.5	Biolegend	100434
CD4	Brilliant Violet 711	Biolegend	100550
CD8	PE Dazzle 594	Biolegend	100762
Foxp3	Alexa Fluor 488	Biolegend	320012
IFNγ	PE/Cy7	Biolegend	505826
IL-17	PE	Biolegend	506933
CD19	Brilliant Violet 650	Biolegend	145517
CD19	biotin	Biolegend	101504
b220	Alexa Fluor 488	Biolegend	103225
b220	PE Dazzle 594	Biolegend	103204
F4/80	Alexa Fluor 488	BioRad	MCA497A488T
CD64	Brilliant Violet 421	Biolegend	139309
CD11b	Brilliant Violet 711	Biolegend	121631
CD11c	Brilliant Violet 785	Biolegend	117336
NK1.1	Brilliant Violet 605	Biolegend	108736
I-A/I-E	Brilliant Violet 510	Biolegend	107636
IL-10	Vio515	Miltenyi Biotec	130-108-097
Gr-1	biotin	Biolegend	108404

Table S4. Gene score list.

apCAF score:

"Cd74", "H2-Aa", "H2-Ab1", "H2-Eb1", "S100a4", "Slpi", "Saa3", "Irf5"

endothelial angiogenesis score:

"Lama4", "Klf6", "Gm1673", "Col14a1", "Hspg2", "Sh3bgrl3", "S100a6", "Col4a2",

"Col4a1", "Rhob", "Lgals1", "Pfn1", "Col15a1", "Serpine1", "Htra1", "Sparc"

Endothelial antigen presentation score:

"Cd74", "Egr1", "Cebpd", "H2-Eb2", "H2-Ea", "Igha", "Cldn5", "Itm2b", "H2-D1",

"H2-Q1", "H2-Q2", "H2-Q4", "H2-Q6", "H2-Q7", "H2-Q10", "Enpp2", "Jam2",

"Sparcl1", "Zc3hav1", "Sertad1", "Jchain", "Cdkn1a", "H2-T24", "H2-T23", "H2-

T22", "Gm11127", "Gm7030", "H2-T10", "Gm8909", "H2-T3", "H2-M10.2", "H2-

M10.1", "H2-M10.3", "H2-M10.4", "H2-M11", "H2-M9", "H2-M1", "H2-M10.5", "H2-

M10.6", "H2-M3", "H2-M2", "H2-M5", "H2-K1", "Socs3", "Cd320", "Irf1", "Fabp5",

"Igfbp2", "Klf4", "Gadd45b"

iCMS2_up:

"Vma21", "Pgrmc1", "Nsdhl", "Gabre", "Lamp2", "Spryd7", "Kpna3", "Tbc1d4",

"Rnaseh2b", "Uchl3", "Myc", "Nkap", "Edn1", "Ccdc85b", "Rnf113a1", "Gm4737",

"Pak1ip1", "C1galt1c1", "Dab2", "Spata13", "Micu2", "Ndfip2", "Prkdc", "Bcap31",

"Commd6", "Mcts1", "Tspan6", "Farp1", "Rpia", "Zdhhc9", "Gm7102", "Ldhb",

"Gal", "Rida", "Ipo5", "Rrs1", "Nit2", "Rbmx2", "Hsd17b10", "Timm8a2",

"Timm8a1", "Ubac2", "Gnpda1", "Gla", "Ftl1-ps1", "Utp14a", "Timp3", "Pdpk1",

"Sox4", "Naa10", "Laptm4b", "Slc7a6", "Hibadh", "Serpine2", "Vbp1", "Nek3",

"Utp4", "Lage3", "Mrpl13", "Cops5", "Prelid3b", "Sinhcaf", "Rrp9", "Utp23", "Nip7",

"AY761185", "Defa21", "Defa23", "Defa35", "Defa25", "Defa38", "Defa30",

"Defa22", "Defa31", "Defa41", "Defa40", "Defa3", "Defa5", "Defa27", "Defa29",

"Defa2", "Defa33", "Defa36", "Defa42", "Defa20", "Defa32", "Defa37", "Defa28",

"Defa43", "Defa26", "Defa17", "Defa34", "Defa39", "Defa24", "Gtf2f2", "Eif3h",

"Rubcnl", "Fundc2", "Pqbp1", "Utp14b", "Cdc16", "C2", "Tsc22d1", "Med30",

"Arl4a", "Exosc5", "Proser1", "Sucla2", "Eif3e", "Dkc1", "Neu1", "Upf3a", "Ddah2",

"Dnajc15", "Zc3h13", "Cyp2s1", "Immp2l", "Capza2", "Trap1", "Dcaf13", "Atp5e",

"Cyb5b", "Pcid2", "Bop1", "Slc52a2", "Cdk4", "Slc3a2", "Top1mt", "Nhlrc3",

"Timm17b", "Malsu1", "Krt23", "Fmr1", "Ccl20", "1110038F14Rik", "Emd",

"Med4", "Txlng", "Prpf6", "Strap", "Tcf7", "Pan3", "Irs2", "Plin2", "Arfgap1",

"Uckl1", "Cdk8", "Mrps31", "Bcl2l1", "Aspscr1", "Plagl2", "Tpd52l2", "Nudt4",

"Avl9", "Fnta", "Rpusd1", "Rnf113a2", "Fbl", "Cars2", "Dnajc5", "Scand1", "Nae1",

"Phf20", "Cdk5rap1", "Ereg", "Igbp1", "Prox1", "Rab20", "Nkd1", "Qprt", "Pdrg1",

"Gpsm2", "Zfp503", "Osbpl2", "Eepd1", "Pofut1", "Mplkip", "Zfand1", "Mapre1",

"Asxl1", "Rnf170", "Gm45692", "Chmp4c", "Fggy", "Uchl4", "Helz2", "Supt20",

"Arfrp1", "Ogfr", "Prr15", "Slc38a5", "Tpx2", "Rnf6", "Ergic3", "Epb41l5", "Trib3",

"Dido1", "Ythdf1", "Ptpro", "Rp9", "Edem2", "Mrgbp", "Ahcy", "Cpne1", "H13",

"Las1l", "Nfs1", "Slc20a2", "Epb41l1", "Abracl", "Psma7", "Gtf3a", "Scarb1",

"Eif6", "Dpep1", "Armc1", "Rbm39", "Prss23", "Commd7", "Adrm1", "Gm9774",

"Pigu", "Csnk2a2", "Dynlrb1", "Cxcl14", "Ctsh", "Gid8", "Trpc4ap", "Golga7",

"Slc29a1", "Tdgf1", "Areg", "Rnf114", "Ctsa", "Snrpb2", "Pet117", "Chchd7",

"Rab5if", "Rab22a", "Naa20", "Ano9", "Smim26", "Tomm34", "Ftl1", "Rpn2",

"Slc5a6", "Psph", "Rtf2", "Cse1l", "Hus1", "Fermt1", "Stx16", "Rb1cc1", "Lypla1",

"Chd6", "Fn1", "Ctnnbl1", "Ascl2", "Aurka", "Uba2", "Nelfcd", "Slc2a8", "Stk4",

"Zmynd8", "Serinc3", "Rae1", "Cct6a", "Atp6v1h", "Gm20716", "Dpm1", "Stau1",

"Txndc9", "Pcif1", "Gm27027", "Alkbh3", "Snrpb", "Cyp2w1", "Acot8", "Pmepa1",

"Ccdc34", "Cebpb", "Atp9a", "Ggh", "Abhd12", "Cox19", "Arhgap45",

"1700037H04Rik", "Plcb4", "Rnf43", "Pcmtd2", "Gtf2ird1", "Axin2", "Xrn2",

"Slc35c2", "Tbrg4", "Ddx27", "Cdc25b", "Eif2s2", "Rprd1b", "Ncoa3", "Ifitm6",

"Gpcpd1", "Pdp1", "Pard6b", "Ndrg3", "Dnttip1", "Pepd", "Vapb", "Mrps17",

"Arid3a", "Esf1", "Ift52", "Blcap", "Ywhab", "Mrps24", "Trp53rka", "Trp53rkb",

"Pfdn4", "Prap1", "Nxt1", "Ube2c", "Ralgapb", "Oser1", "Pltp", "Tnnc2", "Pex16",

"Raly"

iCMS3_up:

"Egln3", "Lpin1", "Try4", "Try5", "Try10", "Prss3", "Gm5771", "Gm10334",

"Prss1", "Prss2", "Dpysl2", "Tymp", "Bnip3l", "9530003J23Rik", "F3", "Clu",

"Ctnnbip1", "Fut8", "Col16a1", "Atl3", "Me1", "Krt7", "Lipg", "Myof", "Pfkp",

"Klk11", "Mmp7", "Cdc42ep1", "Tm4sf4", "Dusp4", "Sytl1", "Tff1", "Sez6l2",

"Depp1", "Rab15", "Adam9", "Ndufa4l2", "Tff2", "Rasl11a", "Ramp1", "Eps8l1",

"Agrn", "Ppp6r1", "S100a13", "Anxa1", "Stim2", "Kdelr3", "Atp1b1", "Rgs10",

"Trim29", "Cd55b", "Cd55", "Pmp22", "Sdr16c5", "Muc5ac", "Dnajc10", "Rgs2",

"Aqp3", "Tmem92", "Serpinb5", "Tpgs1", "Car9", "Cfd", "Tnfrsf26", "Tnfrsf22",

"Tnfrsf23", "Muc3"

Supplementary Materials

Supplementary Figure 1: A distinct cellular and functional landscape of murine primary CRC, liver metastases and peritoneal carcinomatosis

Supplementary Figure 2: Location-specific metabolic reprogramming of the STEM compartment in multivisceral CRC

Supplementary Figure 3: Inter-metastatic differences in stromal cell dynamics during CRC metastasis

Supplementary Figure 4: Location-specific anti-tumoural immunity during CRC metastasis

Supplementary Figure 5: Impairment of B cell networks in metastasized CRC

Supplementary Figure 6: Inter-metastatic alterations of adaptive immune responses multivisceral CRC

Supplementary Figure 7: Murine multivisceral APTKA CRC mimics human stage IV CRC

Supplementary Figure 8: Peritoneal carcinomatosis is associated with a mesenchymal phenotype in human and murine CRC

Supplementary Figure 9: Intraperitoneal application of ICB reconstitutes effector T cell function in PC and emphasizes the importance of site-specific CRC therapy

Table S1. Western Blot Antibody list.

Table S2. IHC Antibody list.

Table S3. Flow cytometry Antibody list.

Table S4. Gene score list.

Movie S1: Orthotopic surgical transplantation of APTKA organoid cells under the serosa of the murine cecum.

Movie S2: Diagnostic laparoscopy eight weeks after orthotopic surgical transplantation of APTKA organoid cells depicting the development of primary tumours, liver metastases and peritoneal carcinomatosis.